Hybrid Power Synchronization Based Transient Stability Enhanced Control for Grid-Forming Inverters Under Symmetrical Grid Fault

Pengfei Sun, Zhen Tian, *Member, IEEE*, Xiaoming Zha, *Member, IEEE*, Meng Huang, *Member, IEEE*, Yibin Tao, Chong Shao, and Xiping Ma

***Abstract*—The current limiter can effectively limit the overcurrent for grid forming (GFM) inverter, but it also makes the inverter easier to lose the stable equilibrium point (SEP) during grid fault. The untimely fault clearing, inaccurate fault depth detection and grid impedance measurement result may lead to overoptimistic deceleration effect evaluation and transient instability problem. In this article, the hybrid power synchronization method is proposed to increase the robustness in transient stability of the GFM inverter against parameters variation. The reactive power that internally related to fault depth is introduced as the dynamic active power reference. It can make sure that the SEP exist during grid fault without the need of fault depth detection. In the same time, the dynamic power compensation related to fault depth is also achieved. The reactive power feedback gain optimization and equivalent power reference limitation method are further given to increase the robustness against large impedance measurement error. Based on equal area criterion, it is demonstrated that with the proposed hybrid power synchronization method, the transient stability of GFM voltage source converter always can be guaranteed once the SEP exists. The impact of line-to-ground fault on transient stability is analyzed and the robust enhanced method is also given. Finally, the effectiveness of the proposed method is verified on a 5 kW experimental platform.**

***Index Terms*—Grid-forming, hybrid power synchronization, overcurrent limitation, transient stability.**

I. Introduction

GRID forming controlled voltage source converter (GFM-VSC) faces severe overcurrent problem under grid fault [1], [2]. Owing to the limit overheat and overcurrent tolerance capability of the power electronic devices, the VSC can only withstand 1.5–2 times overcurrent, then the overcurrent limitation method must be adopted in GFM-VSC [3]. The overcurrent limitation method can be divided into two groups: 1) virtual impedance and 2) current limiter. In contrast with the virtual impedance that indirectly modifies the voltage reference based on voltage loop with low bandwidth in [4] and [5], the current limiter shows better performance in safe, quick, and accurate overcurrent limitation for it can directly limit the current reference based on current loop with high bandwidth [6], [7], [8]. However, the low overcurrent limitation threshold set in current limiter makes the GFM-VSC is easy to lose stable equilibrium point (SEP) during grid fault and further cause transient instability problem [10].

The equal area criterion (EAC) analysis in [11] and [12] shows that the transient stability of GFM-VSC with virtual inertia relies on the existence of SEP and balance between deceleration and acceleration effect. The adaptive damping and inertia control in [13], frequency-voltage feedforward control in [14] and [15], mode adaptive control in [16], and current limitation angle tuning method in [17] were proposed for transient stability enhancement of the GFM-VSC by increasing the work of damping or the deceleration effect. However, the necessity of the existence of SEP during grid fault is overlooked. Once the fault is not cleared in time, the GFM-VSC may lose stable.

To achieve transient stability enhancement under long time grid fault, the virtual power angle estimation method in [18], q-axis voltage feedforward method in [19], adaptive droop gain method in [20] were proposed for the droop-controlled GFM-VSC to make sure that the SEP exist during grid fault. However, the droop-controlled GFM-VSC with no virtual inertia shows overdamping response, as demonstrated in [21]. Once the SEP exists during grid fault, the transient stability of the noninertia GFM-VSC is guaranteed. Therefore, owing to the low requirement in balance between acceleration and deceleration effect, the aforementioned methods cannot be applied in GFM-VSC with virtual inertia.

To achieve transient stability enhancement for GFM-VSC with virtual inertia, the voltage based active power reference decreasing method is proposed in [22] to broaden the deceleration area during grid fault. However, the phase-portrait based design

Received 5 June 2024; revised 23 August 2024; accepted 29 September 2024. Date of publication 14 October 2024; date of current version 18 December 2024. This work was supported by the Science and Technology Project of State Grid Corporation of China under Grant 5419-202355789A-3-8-KJ. Recommended for publication by Associate Editor P. Karamanakos. *(Corresponding authors: Zhen Tian; Xiaoming Zha.)*

Pengfei Sun, Zhen Tian, Xiaoming Zha, and Meng Huang are with the School of Electrical Engineering and Automation, Wuhan University, Wuhan 430072, China, and also with the Key Laboratory of Integrated Energy Power Equipment and System Security, Hubei 430206, China (e-mail: ztian.ee@whu.edu.cn; xmzha@whu.edu.cn).

Yibin Tao is with the Nanjing Research Division of China Electric Power Research Institute, Nanjing 210009, China.

Chong Shao is with the State Grid Gansu Electric Power Company, Gansu 730070, China.

Xiping Ma is with the Electric Power Research Institute, State Grid Gansu Electric Power Company, Gansu 730070, China.

Color versions of one or more figures in this article are available at https://doi.org/10.1109/TPEL.2024.3479325.

Digital Object Identifier 10.1109/TPEL.2024.3479325

method results in heavy work in numerical calculation of the nonlinear equations. The grid impedance estimation accuracy cannot be overlooked such as [23], which may decrease the robustness in transient stability analysis by generating an inaccurate nonlinear model. The grid-code based active power reference tuning method is proposed in [24] for GFM-VSC without grid impedance measurement. However, it cannot be applied to GFM-VSC with current limiter because the reactive power and voltage loop will be saturated by the current limiter [10]. The reactive power synchronization method is proposed in [25] for transient stability enhancement against impedance measurement error. But only fixed reactive power compensation is achieved. Harnefors et al. [26], Kustanovich et al. [27], and Cecati et al. [28] increased the robustness by introducing additional damping or providing the parameters design guideline. However, the high nonlinearity in GFM-VSC during grid fault makes the small signal analysis inaccurate and cannot be applied to the transient stability analysis, as demonstrated in [15]. According to the grid code in China, the asymmetrical grid fault condition still remains a blank part [29]. Therefore, only symmetrical grid fault is considered in this article.

In summary, the transient stability enhancement for GFM-VSC with virtual inertia and current limiter relies on the active power reference tuning. But how to tune it without fault depth detection under line impedance measurement error still remains a difficult task. The hybrid power synchronization method is proposed in this article for transient stability enhancement. The merits are summarized as follows.

1) By introducing the proportional reactive power as active power reference that internally related to fault depth, the dynamic power compensation is achieved without fault depth detection.
2) The reference limitation and reactive power feedback gain optimization method are given to make sure the SEP exist during grid fault against grid impedance estimation error.
3) The EAC analysis shows that based on the proposed hybrid power synchronization method, the transient stability of GFM-VSC always can be guaranteed once the SEP exist under different grid strength and fault depth.
4) The proposed method can be applied both under voltage sags and line-to-ground fault condition without fault types detection, the robust enhanced method is given.

The rest of this article is organized as follows. The modeling and transient instability analysis of GFM-VSC are given in Section II. The proposed hybrid power synchronization method is given in Section III. The impact of line-to-ground fault on transient stability is analyzed and the robust design method is given in Section IV. The experimental verification is given in Section V. Finally, Section VI concludes this article.

II. System Modeling and Transient Instability Problem of GFM-VSC

The modeling and transient stability analysis of GFM-VSC is given in this section.

A. Overall Control Scheme of GFM-VSC

The control scheme and system topology of GFM-VSC is shown in Fig. 1. The GFM-VSC is connected to the large-scaled power system through the connected point. The active power control (APC) loop mimics the rotor function of synchronous generator as (1). P^*, P_e, J, D, and ω_N denotes the active power reference, active power, virtual inertia, damping coefficient, and nominal grid frequency, respectively. The reactive power control (RPC) loop mimics the voltage droop regulation characteristic as (2). Q^*, Q_e, k_q, U_N, and $U_\mathrm{d}{}^*$ denotes the reactive power reference, reactive power, droop coefficient, nominal voltage of GFM-VSC, and d-axis voltage reference, respectively. The virtual power angle is defined as $\delta = \theta_\mathrm{GFM} - \theta_\mathrm{g}$, where θ_GFM and θ_g denotes the phase of GFM-VSC and the voltage U_g. The dc-bus voltage U_dc is viewed as constant. L_g, L_f, C_f, and C_dc denote the line inductance, the inductor, and capacitor filter in the LC filter, and dc-link capacitance, respectively. U_g denote the nominal grid voltage on the connected point. There is $U_\mathrm{g} = U_\mathrm{N}$. The line impedance X_g is viewed as constant because the bandwidth of the APC is very low that the variation of frequency is small. Therefore, there is $X_\mathrm{g} = \omega_\mathrm{N} L_\mathrm{g}$

$$\begin{cases} \dfrac{\mathrm{d}\delta}{\mathrm{d}t} = \omega_\mathrm{GFM} - \omega_\mathrm{N} \\ J\dfrac{\mathrm{d}^2\delta}{\mathrm{d}t^2} = \dfrac{P^*}{\omega_\mathrm{N}} - \dfrac{P_\mathrm{e}}{\omega_\mathrm{N}} - D\cdot\dfrac{\mathrm{d}\delta}{\mathrm{d}t} \end{cases} \tag{1}$$

$$Q_\mathrm{ref} - Q_\mathrm{e} = -k_\mathrm{q}(U_\mathrm{N} - U_\mathrm{d}^*). \tag{2}$$

The cascaded voltage-current control scheme is adopted for the output voltage and current control. The q-axis voltage reference $U_\mathrm{q}{}^* = 0$. k_pv, k_iv, k_pi, and k_ii, denotes the proportional and integral coefficient of PI controller in the voltage loop and current loop. U_d, U_q, I_d, and I_q denotes the dq-axis component in U_GFM and I_g. $I_\mathrm{d}{}^*$ and $I_\mathrm{q}{}^*$ denote the unsaturated current reference in dq-axis. $I_\mathrm{d}{}^{**}$ and $I_\mathrm{q}{}^{**}$ denote the saturated current reference in dq-axis generated by the current limiter. m_d and m_q denote the dq-axis modulation signal generated by the current loop and the m_abc denotes the modulation signal generated by m_d and m_q through Inverse Park transform. The sine pulsewidth modulation is adopted for PWM signal generation

$$S_\mathrm{CS} = \begin{cases} 1, \sqrt{(I_\mathrm{d}^*)^2 + (I_\mathrm{q}^*)^2} \geq I_\mathrm{lim} \\ 0, \sqrt{(I_\mathrm{d}^*)^2 + (I_\mathrm{q}^*)^2} < I_\mathrm{lim} \end{cases} \tag{3}$$

$$\begin{bmatrix} |I_\mathrm{d}^{**}| \\ |I_\mathrm{q}^{**}| \end{bmatrix} = \begin{bmatrix} \min\{|I_\mathrm{d}^*|, I_\mathrm{lim}\} \\ \min\left\{|I_\mathrm{q}^*|, \sqrt{I_\mathrm{lim}^2 - (I_\mathrm{d}^{**})^2}\right\} \end{bmatrix}. \tag{4}$$

The triggering logic of the current limiter is shown in (3), the working principle of the current limiter is shown in (4). S_CS denotes the flag of overcurrent limitation. When $|I_\mathrm{g}| > I_\mathrm{lim}$, the current limiter is triggered, there is $S_\mathrm{CS} = 1$. Otherwise, there is $S_\mathrm{CS} = 0$. Considering the grid code in China as [29], the inverter is required to maintain connected with the faulty grid at least 625 ms with 1.5 p.u. constant overcurrent. Therefore, the current saturation threshold I_lim is set as 1.5 p.u. in this article.

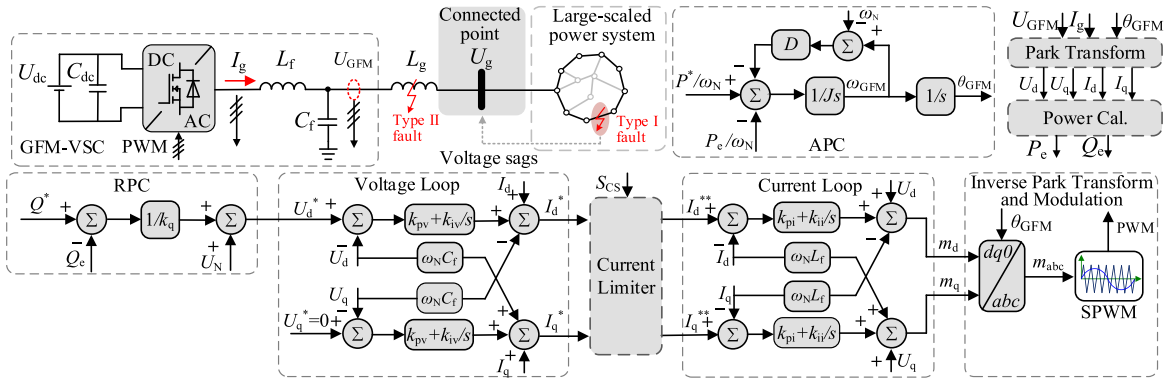

Fig. 1. Overall control structure of GFM-VSC.

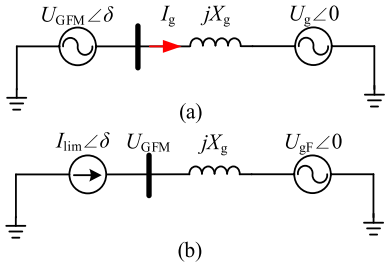

Fig. 2. Single phase equivalent model of GFM-VSC. (a) CUSM. (b) CSM.

In this article, the grid fault is classified into two types as follows.

1) Type I: The short circuit fault occurs within the large scaled power system, which will lead to the voltage sags on the connected point, the grid impedance X_g maintains unchanged.
2) Type II: The short circuit fault occurs just on the transmission line between the VSC and the connected point. The equivalent grid impedance will be significantly decreased and the low voltage will occur on the short circuit point, which will lead to the overcurrent and transient instability problem.

B. Modeling for GFM-VSC Under Type-I Fault

In this section, the modeling and analysis of GFM-VSC under type-I fault is analyzed, the impact of type-II fault on the modeling and analysis is given in Section IV. In the following analysis, the operation mode of GFM-VSC under current limiter triggered is defined as current saturation mode (CSM), the operation mode when current limiter is not triggered is defined as current unsaturation mode (CUSM).

The equivalent circuit of GFM-VSC under CUSM is shown as Fig. 2(a). The voltage loop can work effectively, the output current I_g of GFM-VSC is clamped by the grid voltage and the output voltage of GFM-VSC as

$$I_g\angle\theta_{I_g} = (U_{GFM}\angle\delta - U_g\angle 0)/jX_g. \tag{5}$$

The equivalent circuit of GFM-VSC under CSM is shown as Fig. 2(b). The voltage loop will be saturated owing to the work of current limiter. The output voltage U_{GFM} is clamped by the output current I_g and the grid voltage as

$$U_{GFM}\angle\theta_{U_{GFM}} = U_{gF}\angle 0 + jX_gI_{lim}\angle\delta \tag{6}$$

where the U_{gF} denotes the grid voltage under type-I fault.

The instantaneous output active power P_e and reactive power Q_e of the GFM-VSC can be calculated as

$$\begin{cases} P_e = 1.5U_{GFM}I_g\cos(\theta_{U_{GFM}} - \theta_{I_g}) \\ Q_e = 1.5U_{GFM}I_g\sin(\theta_{U_{GFM}} - \theta_{I_g}) \end{cases} \tag{7}$$

where the θ_{UGFM} and θ_{Ig} denotes the phase of the output voltage U_{GFM} and current I_g in GFM-VSC.

Based on (5)–(7), the active and reactive power of GFM-VSC under CUSM and CSM can be derived as

$$\begin{cases} P_{eCUS} = 1.5U_{GFM}U_g\sin\delta/X_g \\ P_{eCS} = 1.5U_{gF}I_{lim}\cos\delta \end{cases} \tag{8}$$

$$\begin{cases} Q_{eCUS} = 1.5U_{GFM}(U_{GFM} - U_g\cos\delta)/X_g \\ Q_{eCS} = 1.5[I_{lim}^2X_g - U_{gF}I_{lim}\sin\delta] \end{cases} \tag{9}$$

where the P_{eCUS} and P_{eCS} denotes the reactive power of GFM-VSC under CUSM and CSM, Q_{eCUS} and Q_{eCS} denotes the reactive power of GFM-VSC under CUSM and CSM.

C. Transient Instability in GFM-VSC Under Type-I Fault

By applying $d\delta^2/dt^2 = 0$, $d\delta/dt = 0$ and $dP_{eCUS}/d\delta > 0$ in (1), (8), and (9), the power angle δ_S at SEP under CUSM is approximately calculated as (10). By applying $d\delta^2/dt^2 = 0$, $d\delta/dt = 0$, and $dP_{eCS}/d\delta < 0$ in (1) and (8), the power angle δ_{UCS} at the unstable equilibrium point (UEP) under CSM after grid fault is calculated as (11). The impact of RPC is overlooked to get an intuitive view on the SEP distribution in (10). The accurate calculation result considering impact of RPC can also be gotten based on (1)–(2) and (8)–(9)

$$\delta_S \approx \arcsin\left[(2P^*X_g)/\left(3U_g^2\right)\right] \tag{10}$$

$$\delta_{UCS} = \arccos\left[(2P^*)/\left(3U_gI_{lim}\right)\right]. \tag{11}$$

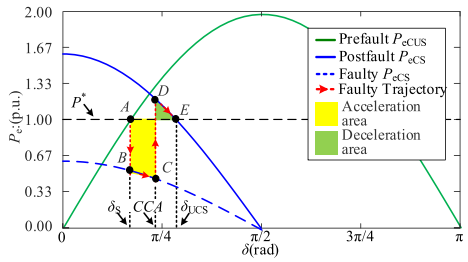

Fig. 3. Power/angle curve of GFM-VSC under type-I fault.

TABLE I
PARAMETERS OF GFM-VSC

Symbol	Value	Symbol	Value
U_{dc}	300 V	J	0.01 W·s^3/rad^2
L_{g1}/ L_{g2}	4.5 mH/1.5 mH	D	0.2 (W·s^2)/rad^2
L_f	1 mH	P*	5 kW
C_f	35 μF	k_q	50
U_g=U_N (V_{rms}, L-L)	80×1.732 V	C_{dc}	1645 μF
ω_N=ω_g	50×2 π rad/s	Q_{ref}	0 Var
k_{pv} , k_{pi}	1, 20	k_{iv} , k_{ii}	20, 100

Fig. 3 shows the trajectory of GFM-VSC under type-I fault. The parameters of GFM-VSC are given in Table I. The prefault P_{eCUS} curve denotes the power angle curve under CUSM before grid fault occur. The postfault P_{eCS} curve denotes the power angle curve under CSM after grid fault is cleared. The faulty P_{eCS} curve denotes the power angle curve under CSM during grid fault. Point A denotes the SEP under nominal grid voltage under CUSM, point C denotes the fault clearing point and E denotes the UEP under CSM during grid fault.

During fault inception, the overcurrent will occur and the current limiter will be triggered, the fault trajectory follows: $A \rightarrow B \rightarrow C \rightarrow D \rightarrow E$. If the EAC is guaranteed as (12), the transient stability of GFM-VSC can be guaranteed. Otherwise, the GFM-VSC cannot decelerate to zero before point E and lose stable

$$\int_{\delta_S}^{CCA} P^* - P_{eCS} \mathrm{d}\delta = \int_{CCA}^{\delta_{UCS}} P_{eCS} - P^* \mathrm{d}\delta. \tag{12}$$

The work of constant positive damping is omitted in (12) because the work of constant positive damping in the GFM-VSC is favorable for transient stability [9], [11].

Based on (12), the critical clearing angle (CCA) can be approximately calculated as

$$\mathrm{CCA} \approx \arcsin\left[\frac{P^*\left(\delta_{UCS}-\delta_S\right)+1.5I_{lim}\left(U_{gF}\sin\delta_S - U_g\sin\delta_{UCS}\right)}{1.5\left(U_{gF}-U_g\right)I_{lim}}\right]. \tag{13}$$

In (13), if the fault is cleared before CCA, the transient stability is guaranteed. When the grid fault is cleared after CCA, the GFM-VSC may lose stable. Moreover, the calculation of δ_S also relies on accurate measurement of line impedance X_g as (10), the inaccurate measurement results also may the inaccurate calculation of CCA and cause the instability problem.

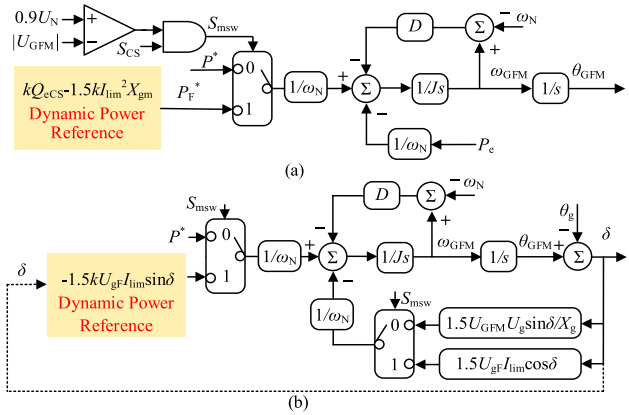

Fig. 4. Control framework of the fundamental hybrid power synchronization method: (a) Control scheme. (b) Large signal model.

Based on (13), the critical clearing time (CCT) can be approximately calculated as (14), as demonstrated in [17]

$$\mathrm{CCT} \approx (\mathrm{CCA}-\delta_S) \times \sqrt{2J \Big/ \int_{\delta_S}^{CCA} \frac{P^*-P_e}{\omega_N}\mathrm{d}\delta}. \tag{14}$$

Based on (10), (11), and (14), the stable operation of GFM-VSC relies on timely fault clearing, accurate grid impedance measurement, and fault depth detection. However, it is usually hard to estimate this information through long transmission line, which result in long transfer delay and low estimation accuracy. This article will focus on how to increase the robustness in transient stability for GFM-VSC against this problem.

III. Hybrid Power Synchronization Based Transient Stability Enhanced Control Under Type-I Fault

In this section, the hybrid power synchronization control is proposed to achieve transient stability enhancement for GFM-VSC during type-I fault against parameters variation.

A. Description of Fundamental Hybrid Power Synchronization

The absence of SEP and transient instability problem during grid fault result from the low active power transfer limit under CSM. By decreasing the active power reference, the SEP can exist during grid fault. But tuning the power reference based on what criterion remains a difficult task. It is better to introduce a variable that internally related to fault depth. Then, the decreasing in active power reference without fault depth detection can be achieved. Then, the hybrid power synchronization method is proposed.

Fig. 4(a) shows the fundamental hybrid power synchronization method. As (15), the proportional reactive power is introduced as the power reference during grid fault. $P_F{}^*$ is defined as the equivalent active power reference. X_{gm} is the measured grid impedance, k denotes the reactive power feedback gain, there is $k > 0$. S_{mSW} denotes the mode switching flag. When the current limiter is triggered and the output voltage magnitude $|U_{GFM}|$ is lower than 0.9 p.u., there is $S_{mSW} = 1$, the active power

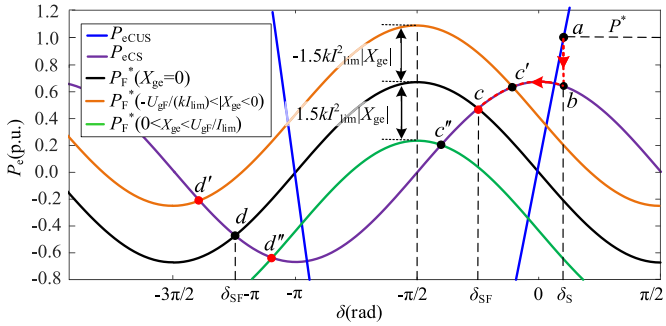

Fig. 5. Robustness in existence of the faulty SEP under a small grid impedance measurement error X_{ge}.

synchronization mechanism is switched into hybrid power synchronization mechanism. After grid fault is cleared, the output voltage magnitude $|U_{GFM}|$ will be higher than 0.9 p.u., there is $S_{mSW} = 0$, the control structure can be switched back to the active power synchronization mechanism

$$P_F^* = kQ_{eCS} - 1.5kI_{lim}^2 X_{gm}. \tag{15}$$

It is assumed that $X_{gm} = X_g$ in (15) at first. Based on (9) and (15), the equivalent active power reference is derived as (16). Then, the large signal model is established in Fig. 5(b)

$$P_F^* = -1.5kU_{gF}I_{lim}\sin\delta. \tag{16}$$

From (16), when the voltage drop is severe, the power reference can automatically be reduced to maintain the transient stability; when the voltage drop is not severe, the amplitude of the power reference $P_F{}^*$ will be lifted. Therefore, the dynamic power compensation is achieved without fault depth detection.

Based on (8) and (16), the power-angle curve of GFM-VSC with hybrid power synchronization mechanism is given in Fig. 5. Point a denotes the SEP under CUSM that satisfies $dP_{eCUS}/d\delta > 0$. Point c denotes the SEP during grid fault that satisfies $dP_{eCS}/d\delta > 0$. Point d denotes the UEP during grid fault that satisfies $dP_{eCS}/d\delta < 0$. During fault inception, the current limiter will be triggered, the trajectory follows: $a \to b \to c \to d \to c$. The period of $c \to d \to c$ results from the virtual inertia of GFM-VSC in (1).

Based on (1), (8), and (16), by applying $d\delta^2/dt^2 = 0$, $d\delta/dt = 0$, and $dP_{eCS}/d\delta > 0$, the power angle δ_{SF} at SEP c with zero grid impedance estimation error can be calculated as

$$\delta_{SF} = -\arctan(1/k). \tag{17}$$

The inequality constraint for SEP exist during grid fault can be provided by the proposed hybrid power synchronization method. It is analyzed based on Intermediate Value Theorem.

Theorem 1 (Intermediate Value Theorem): $f(x)$ is a continuous differentiable function among (m, n), and ξ is any number between $f(m)$ and $f(n)$ that satisfies

$$\min\{f(m), f(n)\} < \xi < \max\{f(m), f(n)\}. \tag{18}$$

If $f(x)$ is a monotonic function among (m, n), then there is only one number $\alpha \in (m, n)$ that satisfies $f(\alpha) = \xi$ as

$$\exists!\alpha \in (m, n), f(\alpha) = \xi. \tag{19}$$

Based on Theorem 1, the difference between the $P_F{}^*$ and the P_{eCS} is defined as $H_e(\delta)$ in

$$H_e(\delta) = P_F^* - P_{eCS}. \tag{20}$$

Based on (8) and (16), $H_e(\delta)$ is a continuous differentiable function keeps monotonically decreasing among $(-\pi/2, 0)$. Let $\xi = 0$. Based on (8), (16), and (20), $H_e(-\pi/2)$, $H_e(0)$ are derived as

$$\begin{cases} H_e(-\pi/2) = -\sqrt{1+k^2}\cdot(-k)/\sqrt{1+k^2} = k > 0 \\ H_e(0) = -\sqrt{1+k^2}\cdot 1/\sqrt{1+k^2} = -1 < 0 \end{cases}. \tag{21}$$

Therefore, there exist only one value δ_{SF} among $(-\pi/2, 0)$ that satisfies $H_e(\delta_{SF}) = 0$, which is the SEP c. It is also easy to demonstrate that there only exist one UEP d among $(-3\pi/2, -\pi)$ following the same way. In summary, no matter what fault depth is, the condition for SEP and UEP exist during grid fault always can be guaranteed. Then, the fault depth detection free is achieved.

The inequality constraint in (21) for SEP exist during grid fault makes the hybrid power synchronization mechanism equipped with a small margin against impedance measurement error.

As Fig. 5, under positive impedance measurement error $|X_{ge}|$, there is $X_{gm} = X_g + |X_{ge}|$. The $P_F{}^*(-\pi/2) = 1.5kU_{gF}I_{lim} - 1.5kI^2_{lim}|X_{ge}|$, $P_{eCS}(-\pi/2) = 0$, When there is $P_F{}^*(-\pi/2) - P_{eCS}(-\pi/2) > 0$, i.e., $|X_{ge}| < U_{gF}/I_{lim}$, the $H_e(-\pi/2) > 0$ can be guaranteed. $P_F{}^*(0) - P_{eCS}(0) = 0\text{-}1.5I^2_{lim}|X_{ge}| < 0$ always can be guaranteed. Therefore, the existence of SEP c'' is guaranteed under a small positive impedance measurement error $|X_{ge}| < U_{gF}/I_{lim}$.

Under negative impedance measurement error $-|X_{ge}|$, there is $X_{gm} = X_g - |X_{ge}|$, the upward movement of $P_F{}^*$ will be as Fig. 5(b). The $P_F{}^*(0) = 1.5kI^2_{lim}|X_{ge}|$, $P_{eCS}(0) = 1.5U_{gF}I_{lim}$. If $|X_{ge}| < U_{gF}/(kI_{lim})$, the $P_F{}^*(0) - P_{eCS}(0) < 0$ can be guaranteed. The $P_F{}^*(-\pi/2) - P_{eCS}(-\pi/2) = 1.5kU_{gF}I_{lim} + 1.5I^2_{lim}|X_{ge}| > 0$ always can be guaranteed. Therefore, the existence of SEP c' is also guaranteed under a small positive impedance measurement error $|X_{ge}| < U_{gF}/(kI_{lim})$. Overall, the hybrid power synchronization method can make sure the SEP exist under small impedance measurement error exist during type-I fault.

B. Robustness Design Against Impedance Measurement Error

Based on the aforementioned analysis, the fundamental hybrid power synchronization mechanism can make sure the SEP exist under small impedance measurement error without fault depth detection. However, the margin is still low. Therefore, in this section, the optimal design method for hybrid power synchronization method against large impedance measurement error is proposed.

1) Reference Limitation for Robustness Enhancement Against Positive Impedance Measurement Error: Under positive impedance measurement error, there is $X_{gm} = X_g + |X_{ge}|$.

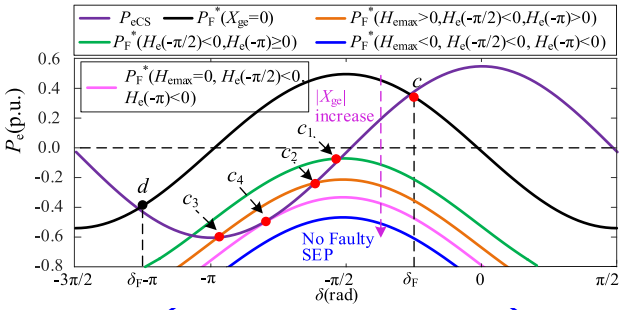

Fig. 6. Impact of large positive impedance measurement error on faulty SEP.

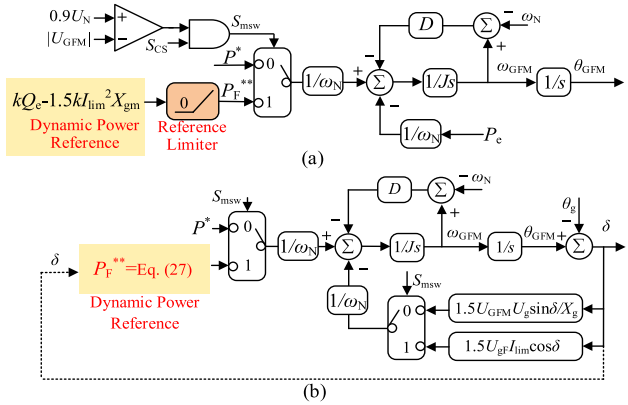

Fig. 7. Control framework of the hybrid power synchronization method with reference limiter. (a) Control scheme. (b) Large signal model.

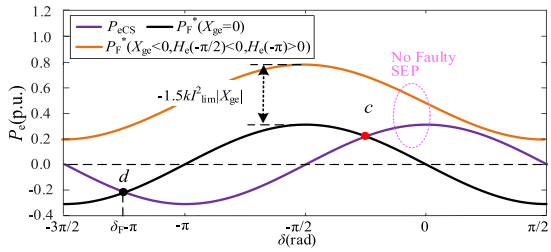

Fig. 8. Impact of large negative impedance measurement error on faulty SEP.

Based on (9) and (15), the power reference can be rewritten as

$$P_{\mathrm{F}}^{*}(\delta) = -1.5kU_{\mathrm{gF}}I_{\mathrm{lim}}\sin\delta - 1.5kI_{\mathrm{lim}}^{2}|X_{\mathrm{ge}}|. \tag{22}$$

In contrast with (16) under $|X_{\mathrm{ge}}| = 0$, the negative dc offset exists in power reference as Fig. 6. If there is (23), the SEP will not exist among $(-\pi/2, 0)$, as demonstrated in Section III-A

$$H_{\mathrm{e}}(-\pi/2) = -1.5kI_{\mathrm{lim}}^{2}|X_{\mathrm{ge}}| - 1.5kU_{\mathrm{gF}}I_{\mathrm{lim}} < 0. \tag{23}$$

For the $H_{\mathrm{e}}(-\pi)$, which can be analyzed into two conditions.

1) If $H_{\mathrm{e}}(-\pi)\geq 0$, the SEP c_1 exist among $(-\pi, -\pi/2)$, which satisfies $P_{\mathrm{eCS}} < 0$, the inverse power transfer will lead to overvoltage in dc-link because both the dc-side and ac side inject power into the dc-link capacitance.
2) If $H_{\mathrm{e}}(-\pi) > 0$, $H_{\mathrm{e}}(\delta)$ is a nonmonotonic function among $(-\pi, -\pi/2)$. There is $\mathrm{d}H_{\mathrm{e}}(\delta)/\mathrm{d}\delta = -1.5U_{\mathrm{gF}}I_{\mathrm{lim}}(k\cos\delta - \sin\delta)$. It has zero-crossing point $\delta = \arctan k - \pi$ among $(-\pi, -\pi/2)$. $\delta \in (-\pi, \arctan k - \pi)$, $\mathrm{d}H_{\mathrm{e}}(\delta)/\mathrm{d}\delta > 0$. $\delta \in (\arctan k - \pi, -\pi/2)$, $\mathrm{d}H_{\mathrm{e}}(\delta)/\mathrm{d}\delta < 0$. Then, the $H_{\mathrm{e}}(\delta)$ will first increasing and then decreasing among $(-\pi, -\pi/2)$, then, it can be analyzed into two conditions.
3) When $H_{\mathrm{emax}} < 0$, then there exist no SEP among $(-\pi, -\pi/2)$, then the transient instability problem will occur.
4) When $H_{\mathrm{emax}} > 0$, then the SEP: c_2 and c_3 exist among $(-\pi, -\pi/2)$ and the inverse power transfer occur. When $H_{\mathrm{emax}} = 0$, c_2 and c_3 converge to point c_4 and the instability problem occur.

The H_{emax} is the maximum value of $H_{\mathrm{e}}(\delta)$, there is $H_{\mathrm{emax}} = H_{\mathrm{e}}(\arctan k - \pi) - 1.5kI^{2}{}_{\mathrm{lim}}|X_{\mathrm{ge}}|$. Overall, the transient instability or inverse power transfer occur when (23) is satisfied.

Considering $k > 0$, $I_{\mathrm{lim}} > 0$, the (23) can be rewritten as

$$U_{\mathrm{gF}} - I_{\mathrm{lim}}X_{\mathrm{ge}} < 0. \tag{24}$$

From (24), the resulted negative power reference or absence of SEP is only related with the fault depth U_{gF}, current limitation threshold I_{lim}, and the impedance measurement error $|X_{\mathrm{ge}}|$. The lower U_{gF} and the larger X_{ge} will increase the risk of steady-state negative power reference at the faulty SEP. To prevent the negative power reference or absence of SEP under positive impedance measurement error. The reference limiter is introduced as (25), the control scheme is depicted as Fig. 7(a)

$$P_{\mathrm{F}}^{**} = \max\{P_{\mathrm{F}}^{*}, 0\} \tag{25}$$

where the $P_{\mathrm{F}}{}^{**}$ denotes the power reference generated by the reference limiter. The working principle is: If the power reference $P_{\mathrm{F}}{}^{*}$ is lower than zero, the reference is limited as zero. Otherwise, the power reference $P_{\mathrm{F}}{}^{*}$ maintains unchanged. Overall, the negative power reference can be prevented.

Based on (8), (9), and (25), the equivalent power reference with reference limiter can be derived as (26) under $|X_{\mathrm{ge}}| = 0$

$$P_{\mathrm{F}}^{**} = \begin{cases} -1.5U_{\mathrm{gF}}I_{\mathrm{lim}}\sin\delta, \delta \in [-\pi, 0] \\ 0, \delta \in (0, \pi/2) \cup (-3\pi/2, -\pi) \end{cases}. \tag{26}$$

Based on (8)–(9) and (26), the large signal model of the hybrid power synchronization control with power reference limiter is reshaped as Fig. 7(b). The corresponding impact on transient stability will be analyzed in the following section.

2) Reactive Power Feedback Gain Design for Robustness Enhancement Against Negative Impedance Measurement Error: Under negative impedance measurement error condition, there is $X_{\mathrm{gm}} = X_{\mathrm{g}} - |X_{\mathrm{ge}}|$. Then, the equivalent power reference with negative impedance measurement error is rewritten as (27) based on (9) and (15)

$$P_{\mathrm{F}}^{*}(\delta) = -1.5kU_{\mathrm{gF}}I_{\mathrm{lim}}\sin\delta + 1.5kI_{\mathrm{lim}}^{2}|X_{\mathrm{ge}}|. \tag{27}$$

In contrast with the power reference under $|X_{\mathrm{ge}}| = 0$ in (16), the positive dc offset in power reference will occur as Fig. 8. The condition for SEP exists among $(-\pi/2, 0)$ is given as (28) according to Theorem 1 considering the constraint $\mathrm{d}P_{\mathrm{eCS}}/\mathrm{d}\delta > 0$

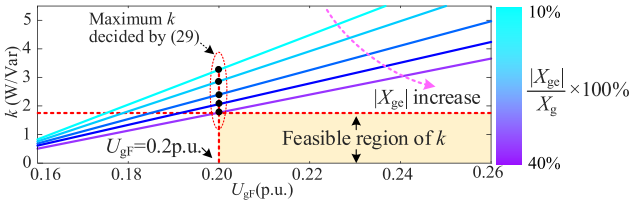

Fig. 9. Feasible region of reactive power feedback coefficient k.

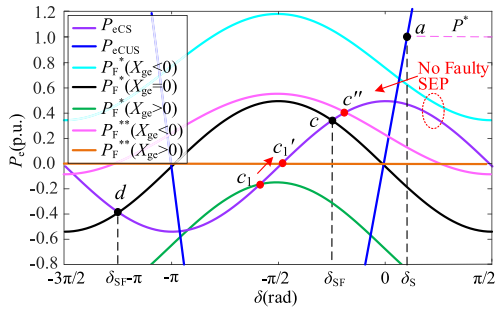

Fig. 10. Impact of power reference limiter and power feedback coefficient k optimization on power angle curve.

and $P_{\mathrm{eCS}} > 0$

$$\begin{cases} H_{\mathrm{e}}\left(-\pi/2\right) = 1.5kU_{\mathrm{gF}}I_{\mathrm{lim}} + 1.5kI_{\mathrm{lim}}^2\left|X_{\mathrm{ge}}\right| > 0 \\ H_{\mathrm{e}}\left(0\right) = 1.5kI_{\mathrm{lim}}^2\left|X_{\mathrm{ge}}\right| - 1.5U_{\mathrm{gF}}I_{\mathrm{lim}} < 0. \end{cases} \tag{28}$$

The first inequality in (28) always can be guaranteed, then based on the second inequality in (28) is satisfied, the boundary of reactive power feedback gain k is derived as (29)

$$0 < k < U_{\mathrm{gF}}/(|X_{\mathrm{ge}}|\, I_{\mathrm{lim}}). \tag{29}$$

Based on (29), the upper boundary of reactive power feedback coefficient k is designed according to the deepest fault depth U_{gF} required by the grid code in China in [29] and the largest impedance measurement error provided by the method such as [23], which is shown in Fig. 9. In this article, the deepest $U_{\mathrm{gF}} = 0.2$ p.u., as recommended in [29], and 40% impedance measurement accuracy is selected as an example in design of the upper boundary of k. $k < 1.7$ is selected in this article under the short circuit ratio is 2.7.

Fig. 10 further shows the impact of reference limiter and coefficient k optimization on power-angle curve and equivalent active power reference distribution. When the too large negative impedance measurement error occurs, by decreasing the coefficient k according to (29), the upward movement in the power reference can be mitigated and the SEP c'' can be guaranteed. When the too large positive impedance measurement error occurs, the reference limiter will be activated and the SEP c_1 will move to point c_1' with $P_{\mathrm{eCS}} = 0$. Which means that the non-negative power reference is guaranteed and the induced power backflow and overvoltage in dc-link can be prevented. Moreover, the absence of SEP also can be prevented.

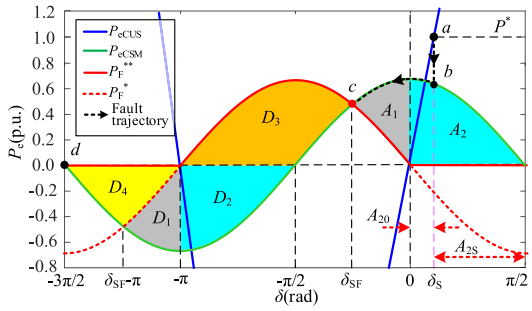

Fig. 11. Acceleration and deceleration area distribution in hybrid power synchronization control.

C. Transient Stability Analysis Using Equal Area Criterion

The transient stability of GFM-VSC only can be guaranteed with SEP exist and the balance between deceleration and acceleration area is satisfied. In the aforementioned analysis, the robustness for SEP exist against impedance measurement error is enhanced. The balance between the acceleration and deceleration area is analyzed in this section.

Fig. 11 shows the equivalent fault trajectory of the GFM-VSC with hybrid power synchronization method. To simplify the analysis, the fault trajectory still follows the active power curve under CSM, and the power reference is analyzed based on (25)–(26). The original nominal operation point of the GFM-VSC is defined as point a. During grid fault inception, the trajectory follows: $a \to b \to c \to d \to$c. The period of $c \to d \to$c results from the virtual inertia in GFM-VSC. The deceleration area can be divided into four parts: D_1, D_2, D_3, and D_4. The acceleration area can be divided into two parts as: A_1 and A_{20}.

The prefault power angle δ_{S} at SEP a will be changed under different grid strength. Considering the constraint $\mathrm{d}P_{\mathrm{eCUS}}/\mathrm{d}\delta > 0$, there is $\delta_{\mathrm{S}} \in (0, \pi/2)$ the SEP a. Then, the δ_{S} is scaled to $\pi/2$ and the acceleration area is expanded from A_{20} to A_2 as

$$\begin{aligned} A_{20} &= \int_0^{\delta_{\mathrm{S}}} 1.5U_{\mathrm{gF}}I_{\mathrm{lim}}\cos\delta - 0\mathrm{d}\delta \\ < A_2 &= A_{20} + A_{2\mathrm{S}} = \int_0^{\pi/2} 1.5U_{\mathrm{gF}}I_{\mathrm{lim}}\cos\delta - 0\mathrm{d}\delta \end{aligned} \tag{30}$$

where the $A_{2\mathrm{S}}$ denotes the scaled calculation part of the acceleration area. The A_{20} denotes the original acceleration area. The scaled calculation of acceleration area will not violent the transient stability, but only increase the robustness of the hybrid power synchronization method.

It is easy to obtain that the deceleration effect in D_1 is equal to the acceleration effect in A_1 as (31). The deceleration effect in D_2 is also equal to the acceleration effect in A_2 as

$$\begin{aligned} A_1 &= \int_{\delta_{\mathrm{SF}}}^{0} 1.5U_{\mathrm{gF}}I_{\mathrm{lim}}\cos\delta + 1.5kU_{\mathrm{gF}}I_{\mathrm{lim}}\sin\delta\mathrm{d}\delta \\ &= D_1 = \int_{-\pi}^{\delta_{\mathrm{SF}}-\pi} 1.5kU_{\mathrm{gF}}I_{\mathrm{lim}}\sin\delta + 1.5U_{\mathrm{gF}}I_{\mathrm{lim}}\cos\delta\mathrm{d}\delta \end{aligned} \tag{31}$$

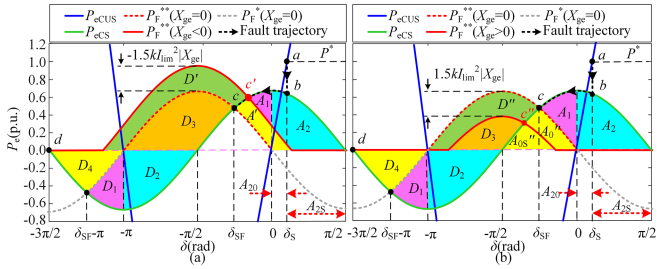

Fig. 12. Acceleration and deceleration area distribution in hybrid power synchronization mechanism with grid impedance measurement error. (a) With negative measurement error. (b) With positive measurement error.

$$A_2 = \int_0^{\pi/2} 1.5U_{\mathrm{gF}}I_{\mathrm{lim}}\cos\delta - 0\mathrm{d}\delta$$
$$= D_2 = \int_{-\pi}^{-\pi/2} 0 - 1.5U_{\mathrm{gF}}I_{\mathrm{lim}}\cos\delta\mathrm{d}\delta. \quad (32)$$

Therefore, by adopting the hybrid power synchronization method, the EAC can always be guaranteed with extra deceleration area D_3 and D_4 left as (33). The left side in (33) denotes the whole acceleration effect and the right side in (33) denotes the whole deceleration effect. Therefore, the transient stability of GFM-VSC can be enhanced

$$A_1 + A_2 < D_1 + D_2 + D_3 + D_4. \quad (33)$$

Besides, it is demonstrated in [30] that the work of damping is equivalent to add an extra deceleration area during large disturbance. Therefore, the robustness of the proposed hybrid power synchronization method is further enhanced without considering work of constant positive damping in (33).

As Fig. 12(a), considering the condition with negative impedance measurement error, the upward move in equivalent power reference will be, which will generate an extra deceleration area D'. The acceleration area A' will be loss. Therefore, the transient stability demonstration in (33) will not be violated.

As Fig. 12(b), considering the condition with positive impedance measurement error, the downward move in power reference will be. It will lead to the loss in the deceleration area D'', the acceleration area will be expanded with an extra area $A_0{}''$. The original acceleration equality relationship between A_1 and D_1, A_2 and D_2 will not be violented.

It is easy to obtain that the deceleration effect in area D_4 equals to the acceleration effect in area $A_0{}''$ and $A_{0\mathrm{S}}{}''$ as (34). The area $A_{0\mathrm{S}}{}''$ denotes the scaled calculation of acceleration area. The area $A_0{}''$ denotes the real extra acceleration area generated by positive grid impedance measurement error

$$D_4 = \int_{-3/2\pi}^{\delta_{\mathrm{SF}}-\pi} -1.5U_{\mathrm{gF}}I_{\mathrm{lim}}\cos\delta\mathrm{d}\delta + \int_{\delta_{\mathrm{SF}}-\pi}^{-\pi} 1.5kU_{\mathrm{gF}}I_{\mathrm{lim}}\sin\delta\mathrm{d}\delta$$
$$\geq A''_0 + A''_{0\mathrm{S}} = \int_{-\pi/2}^{\delta_{\mathrm{SF}}} 1.5U_{\mathrm{gF}}I_{\mathrm{lim}}\cos\delta\mathrm{d}\delta$$
$$+ \int_{\delta_{\mathrm{SF}}-\pi}^{-\pi} 1.5kU_{\mathrm{gF}}I_{\mathrm{lim}}\sin\delta\mathrm{d}\delta. \quad (34)$$

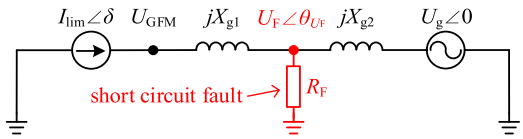

Fig. 13. Equivalent single-phase circuit under type-II fault.

Therefore, the EAC can also be guaranteed as (35). It means that the transient stability of GFM-VSC also can be guaranteed with positive impedance measurement error. The scaled calculation of acceleration area also only increased the robustness in transient stability margin

$$A''_{0\mathrm{S}} + A_0{}'' + A_1 + A_2 < D_1 + D_2 + D_3 + D_4. \quad (35)$$

IV. Robust Enhanced Design Under Type-II Fault

In this section, the impact of type-II fault on transient stability is analyzed, the robust enhanced method is given.

A. Power Angle Characteristic Modeling Under Type-II Fault

The single-phase equivalent circuit for GFM-VSC under type-II fault is shown as Fig. 13. The fault resistance R_{F} will lead to a low voltage U_{F} at the fault point and transient instability problem. X_{g1} and X_{g2} denotes the VSC and grid side line impedance as (36). σ denotes the ratio between X_{g1} and X_{g}

$$X_{\mathrm{g1}} = \sigma\cdot X_{\mathrm{g}}, X_{\mathrm{g2}} = (1-\sigma)\cdot X_{\mathrm{g}}, \sigma\in(0,1). \quad (36)$$

Different from the type-I fault, the grid voltage U_{g} is viewed as constant as 1.0 p.u. under type-II fault because owing to the limit capacity of the VSC, the voltage in the large scaled power system can hardly be affected by VSC. Then, the function of voltage $U_{\mathrm{F}}\angle\theta_{UF}$ at the short circuit point, grid voltage $U_{\mathrm{g}}\angle 0$ and output current of GFM-VSC $I_{\mathrm{lim}}\angle\delta$ is established as

$$(1/R_{\mathrm{F}} + 1/jX_{\mathrm{g2}})\cdot U_{\mathrm{F}}\angle\theta_{U_{\mathrm{F}}} - (1/jX_{\mathrm{g2}})\cdot U_{\mathrm{g}}\angle 0 = I_{\mathrm{lim}}\angle\delta \quad (37)$$

where the U_{F} denotes the voltage amplitude at the fault point, θ_{UF} denotes its phase. Then, the output voltage of GFM-VSC is derived as

$$U_{\mathrm{GFM}}\angle\theta_{U_{\mathrm{GFM}}} = U_{\mathrm{F}}\angle\theta_{U_{\mathrm{F}}} + jX_{\mathrm{g1}}\cdot I_{\mathrm{lim}}\angle\delta. \quad (38)$$

Based on (7), (37)–(38), the active and reactive power of GFM-VSC under type-II fault can be derived as

$$P_{\mathrm{eCS-SC}} = \underbrace{\frac{3}{2}\cdot\frac{R_{\mathrm{F}}U_{\mathrm{g}}I_{\mathrm{lim}}\cos(\delta+\varphi_1)}{\sqrt{R_{\mathrm{F}}^2+X_{\mathrm{g2}}^2}}}_{P_{\mathrm{eCS-SC-ac}}} + \underbrace{\frac{3}{2}\cdot\frac{I_{\mathrm{lim}}^2X_{\mathrm{g2}}^2R_{\mathrm{F}}}{R_{\mathrm{F}}^2+X_{\mathrm{g2}}^2}}_{P_{\mathrm{eCS-SC-dc}}} \quad (39)$$

$$Q_{\mathrm{eCS-SC}} = \underbrace{\frac{3I_{\mathrm{lim}}^2}{2}\left[X_{\mathrm{g1}} + \frac{X_{\mathrm{g2}}R_{\mathrm{F}}^2}{R_{\mathrm{F}}^2+X_{\mathrm{g2}}^2}\right]}_{Q_{\mathrm{eCS-SC-dc}}} - \underbrace{\frac{3R_{\mathrm{F}}U_{\mathrm{g}}I_{\mathrm{lim}}\sin(\delta+\varphi_1)}{2\sqrt{R_{\mathrm{F}}^2+X_{\mathrm{g2}}^2}}}_{Q_{\mathrm{eCS-SC-ac}}} \quad (40)$$

$$\varphi_1 = \arctan\left(X_{g2}/R_F\right) \in (0, \pi/2) \tag{41}$$

where $P_{eCS\text{-}SC}$ and $Q_{eCS\text{-}SC}$ denotes the active and reactive power under type-II fault, $P_{eCS\text{-}SC\text{-}ac}$ and $P_{eCS\text{-}SC\text{-}dc}$ denotes the ac and dc offset component in $P_{eCS\text{-}SC}$. $Q_{eCS\text{-}SC\text{-}ac}$ and $Q_{eCS\text{-}SC\text{-}dc}$ denotes the ac and dc offset component in $Q_{eCS\text{-}SC}$. The R_F, X_{g1} and X_{g2} are hardly to obtain during fault inception, making the CCT calculation unable to be carried out with the same method in Section II-C.

The maximum value of $P_{eCS\text{-}SC\text{-}dc}$ and $Q_{eCS\text{-}SC\text{-}dc}$ satisfies (42)–(43), which is demonstrated in the Appendix

$$Q_{eCS-SC-dc} < 1.5 I_{lim}^2 X_g \tag{42}$$

$$P_{eCS-SC-dc} \le 0.75 I_{lim}^2 X_g. \tag{43}$$

B. Impact of Type-II Fault on Transient Stability Analysis

Based on (15) and (40), the equivalent active power reference $P_F{}^*$ is rewritten as (44). Based on (42) and (44), the negative dc offset in $P_F{}^*$ is introduced. Then, the power reference with limiter ($P_F{}^{**}$) and the EAC demonstration is mainly analyzed under the condition with positive grid impedance measurement as in Section IV-C.

It should be noted that the fault resistance R_F usually is a very small value, then the $Q_{eCS\text{-}SC\text{-}dc}$ is actually far less than $1.5I^2{}_{lim}X_g$. Therefore, under type-II fault, the fault resistance R_F instead of the impedance measurement error plays as the dominant role in equivalent change in line impedance, then $X_{gm} = X_g$ is adopted for analysis

$$P_F^* = kQ_{eCS-SC-ac} + \underbrace{k \cdot \left[Q_{eCS-SC-dc} - 1.5 I_{lim}^2 X_g\right]}_{<0}. \tag{44}$$

The zero-crossing points of the active power under type-II fault are denoted as δ_{ZC1} and δ_{ZC2}, which can be calculated as (45) by applying the constraint $P_{eCS\text{-}SC} = 0$ in (39)

$$\delta_{ZC1,2} = \pm \arccos\left[-\left(I_{lim}X_{g2}^2\right) \Big/ \left(U_g\sqrt{R_F^2 + X_{g2}^2}\right)\right] - \varphi_1. \tag{45}$$

There is $\delta_{ZC1} \in (0, \pi)$, $\delta_{ZC2} \in (-3\pi/2, -\pi/2)$. Then, the impact of type-II fault on the transient stability of GFM-VSC with the hybrid power synchronization method can be analyzed into three conditions: $\delta_S < \delta_{ZC1}$, $\delta_S > \delta_{ZC1}$, and $\delta_S = \delta_{ZC1}$.

1) Under $\delta_S < \delta_{ZC1}$, the $P_F{}^{**} < P_{eCS\text{-}SC}$ During Fault Inception Will be, Leading to Negative $d^2\delta/dt^2$ and Decrease in Power Angle.: The fault trajectory follows: $a \to b \to c \to d \to c$ as Fig. 14. Point c and d denotes the faulty SEP and UEP. The deceleration area includes D_{EC} and D_0, the acceleration area includes: A_{CC} and A_S. Actually, A_S is neither the acceleration area nor the deceleration area, it is just adopted for simplify the EAC demonstration. The dc offset in active power will increase the acceleration area and decrease the deceleration area compared with the type-I fault condition. The largest acceleration area and minimum deceleration area is calculated as (46)–(47) by viewing the power reference $P_F{}^{**}$ as zero, i.e., D_0 is viewed as zero. The start point of area A_{CC} is scaled from δ_S to δ_{ZC1} in

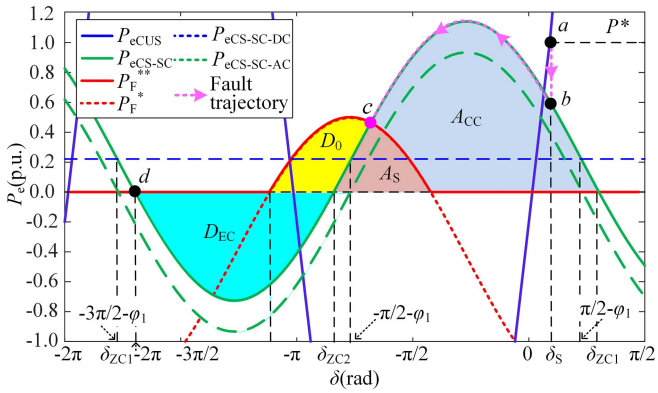

Fig. 14. Deceleration and acceleration area distribution with hybrid power synchronization method under $\delta_S < \delta_{ZC1}$.

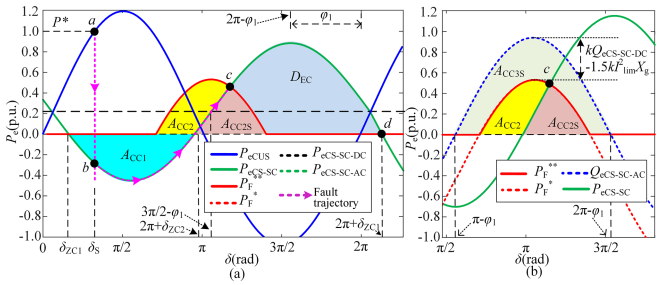

Fig. 15. Deceleration and acceleration area distribution with hybrid power synchronization method under $\delta_S < \delta_{ZC1}$. (a) Envelope view. (b) Zoom-in view.

(46) to obtain the largest acceleration area

$$A_S + A_{CC} = \int_{\delta_{ZC2}}^{\delta_{ZC1}} P_{eCS-SC-ac} + P_{eCS-SC-dc} - 0 \mathrm{d}\delta \tag{46}$$

$$D_{EC} = \int_{\delta_{ZC1}-2\pi}^{\delta_{ZC2}} 0 - \left(P_{eCS-SC-ac} + P_{eCS-SC-dc}\right) \mathrm{d}\delta. \tag{47}$$

Based on (46)–(47), the maximum increased extra acceleration area under type-II fault is calculated as

$$A_S + A_{CC} - D_{EC} = \int_{\delta_{ZC1}-2\pi}^{\delta_{ZC1}} P_{eCS-SC-dc} - 0 \mathrm{d}\delta. \tag{48}$$

2) Under $\delta_S > \delta_{ZC1}$, the $P_F{}^{**} > P_{eCS\text{-}SC}$ Will be, Then, the Positive $d^2\delta/dt^2$ Will be, Leading to the Increase in Power Angle.: The fault trajectory follows: $a \to b \to c \to d \to c$ as Fig. 15. Point c and d denotes the faulty SEP and UEP. The acceleration area is divided into three parts: A_{CC1}, A_{CC2}, and A_{CC2S}, the deceleration area is divided into two parts: D_{EC} and A_{CC2S}. Actually, A_{CC2S} is neither the real acceleration area nor the deceleration area, it is just adopted for simplify the EAC demonstration.

The A_{CC1} and D_{EC}+A_{CC2S} is scaled calculated as

$$A_{CC1} = \int_{\delta_{ZC1}}^{2\pi+\delta_{ZC2}} 0 - \left(P_{eCS-SC-ac} + P_{eCS-SC-dc}\right) \mathrm{d}\delta \tag{49}$$

$$D_{\mathrm{EC}} + A_{\mathrm{CC2S}} = \int_{2\pi+\delta_{\mathrm{ZC2}}}^{2\pi+\delta_{\mathrm{ZC1}}} \left(P_{\mathrm{eCS-SC-ac}} + P_{\mathrm{eCS-SC-ac}}\right) - 0\mathrm{d}\delta. \tag{50}$$

Therefore, when only considering the area A_{CC1} and D_{EC}+A_{CC2S}, the extra deceleration area is introduced as

$$D_{\mathrm{EC}} + A_{\mathrm{CC2S}} - A_{\mathrm{CC1}} = \int_{\delta_{\mathrm{ZC1}}}^{2\pi+\delta_{\mathrm{ZC1}}} P_{\mathrm{eCS-SC-dc}} - 0\mathrm{d}\delta > 0. \tag{51}$$

The amplitude of $Q_{\mathrm{eCS\text{-}SC\text{-}ac}}$ satisfies (52) based on (40)

$$\left|-1.5R_{\mathrm{F}}U_{\mathrm{g}}I_{\mathrm{lim}}\Big/\sqrt{R_{\mathrm{F}}^2+X_{\mathrm{g2}}^2}\right| < \left|-1.5U_{\mathrm{g}}I_{\mathrm{lim}}\right|. \tag{52}$$

Based on (52), the maximum acceleration area A_{CC2} and A_{CC2S} is scaled calculated as

$$\begin{aligned} &A_{\mathrm{CC2}} + A_{\mathrm{CC2S}} < A_{\mathrm{CC2}} + A_{\mathrm{CC2S}} + A_{\mathrm{CC3S}} \\ &= \int_{\pi-\varphi_1}^{2\pi-\varphi_1} kQ_{\mathrm{eCS-SC-ac}}\mathrm{d}\delta \\ &< \int_{\pi-\varphi_1}^{2\pi-\varphi_1} -1.5kU_{\mathrm{g}}I_{\mathrm{lim}}\sin\left(\delta+\varphi_1\right)\mathrm{d}\delta. \end{aligned} \tag{53}$$

In (53), the A_{CC3S} denotes the scaled calculation area of the acceleration area in Fig. 15(b). Obviously, there is $A_{\mathrm{CC3S}} > 0$ owing to the negative dc offset in (44).

Then, the largest increased acceleration area can be obtained as (54) by omitting the extra deceleration area in (51) and only considering the largest extra acceleration area in (53)

$$\begin{aligned} &A_{\mathrm{CC2}} + A_{\mathrm{CC1}} - D_{\mathrm{EC}} = \left(A_{\mathrm{CC2}} + A_{\mathrm{CC2S}}\right) \\ &\quad - \left[D_{\mathrm{EC}} + A_{\mathrm{CC2S}} - A_{\mathrm{CC1}}\right] < \left(A_{\mathrm{CC2}} + A_{\mathrm{CC2S}}\right) \\ &< A_{\mathrm{CC2}} + A_{\mathrm{CC2S}} + A_{\mathrm{CC3S}} \end{aligned} \tag{54}$$

3) If $\delta_S = \delta_{ZC1}$, There Will be no Transient Nonlinear Process in Synchronization Loop Because There is $\mathrm{P}^*_{F\text{-}REB} = \mathrm{P}_{eCS}$*.:* However, this condition is very rare for its strict equality constraints.

C. Modified Hybrid Power Synchronization Control for Transient Stability Enhancement

1) Modified Hybrid Power Synchronization Control Scheme: To mitigate the extra acceleration area under type-II fault in (48) and (54), the extra power reference $P_{\mathrm{REB}}{}^*$ is introduced by the robust enhanced branch as (55). The control scheme is given in Fig. 16. In (55), k_1, k_2, and k_3 denotes the feedback coefficient. There is $k_1 < 0$, $k_2 > 0$, and $k_3 > 0$. S_{msw} has the same meaning as Fig. 5. There is $P_{\mathrm{REB}}{}^* = 0$ among $(0, \pi/2)$, then the stability analysis based on zero-crossing points in Section IV-B is not violated

$$P^*_{\mathrm{REB}} = \begin{cases} \max\left\{k_1\cdot|\delta+\pi| - k_1\pi/2, 0\right\}, \delta < 0 \\ 0, \pi/2 > \delta \geq 0 \\ -k_3\cdot(\delta - 3\pi/2), 3\pi/2 > \delta \geq \pi/2 \\ \max\left\{k_2\cdot|\delta-2\pi| - k_2\pi/2, 0\right\}, \text{else}. \end{cases} \tag{55}$$

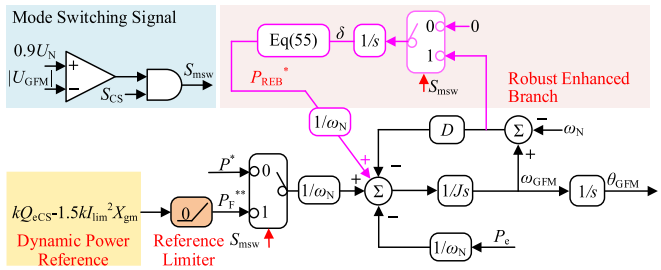

Fig. 16. Hybrid power synchronization with robustness enhanced branch.

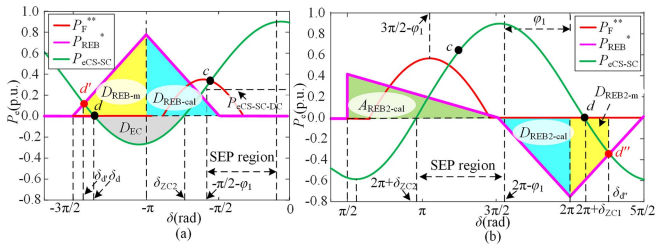

Fig. 17. Power angle curve of the modified hybrid power synchronization method under type-II fault. (a) $\delta_S < \delta_{ZC1}$. (b) $\delta_S > \delta_{ZC1}$.

In (55), the power angle δ is generated by the integral result of the frequency difference as (56). 1/s denotes the integral term

$$\delta = \left(\omega_{\mathrm{GFM}} - \omega_{\mathrm{N}}\right)/s. \tag{56}$$

Then, the power reference of the hybrid power synchronization method with robust enhanced branch is denoted as $P^*{}_{\mathrm{F\text{-}wREB}}$ as

$$P^*_{\mathrm{F-wREB}} = P^*_{\mathrm{REB}} + P^{**}_{\mathrm{F}}. \tag{57}$$

Based on (56)–(57), the power angle curve of the hybrid power synchronization mechanism with robust enhanced branch is given in Fig. 17. The detailed analysis are given in the following analysis.

2) Demonstration of the Existence of Faulty SEP: The condition for SEP exists is still demonstrated based on Theorem 1. $H_{\mathrm{eSC}}(\delta)$ is defined as the difference between the active power reference $P^*{}_{\mathrm{F\text{-}wREB}}$ and the active power $P_{\mathrm{eCS\text{-}SC}}$ under type-II fault as

$$H_{\mathrm{eSC}}\left(\delta\right) = P^*_{\mathrm{F-wREB}} - P_{\mathrm{eCS-SC}}. \tag{58}$$

The $H_{\mathrm{eSC}}(\delta)$ is further divided into $H_{\mathrm{eSC\text{-}ac}}(\delta)$ and $H_{\mathrm{e\text{-}SC\text{-}dc}}(\delta)$ as (59) based on (15), (39) and (57)–(58)

$$\begin{cases} H_{\mathrm{eSC-ac}}\left(\delta\right) = P^{**}_{\mathrm{F}} - P_{\mathrm{eCS-SC-ac}} \\ H_{\mathrm{eSC-dc}}\left(\delta\right) = -P_{\mathrm{eCS-SC-dc}} + P^*_{\mathrm{REB}} \end{cases}. \tag{59}$$

Under $\delta_S > \delta_{ZC1}$, considering $\mathrm{d}P_{\mathrm{eCS\text{-}SC}}/\mathrm{d}\delta > 0$ and $P_{\mathrm{eCS}} > 0$, the SEP may be located among $(-\pi/2\ -\varphi_1, -\varphi_1)$. Obviously, $H_{\mathrm{eSC}}(\delta)$ is a monotonically decreasing function among $(-\pi/2\ -\varphi_1, -\varphi_1)$. Based on (39)–(40) and (57)–(59), the value of $H_{\mathrm{eSC\text{-}ac}}(-\pi/2\ -\varphi_1)$, $H_{\mathrm{eSC\text{-}ac}}(-\varphi_1)$ and $H_{\mathrm{eSC\text{-}dc}}(-\varphi_1)$ are

given as

$$\begin{cases} H_{\mathrm{eSC-ac}}(-\varphi_1) = -1.5R_{\mathrm{F}}U_{\mathrm{g}}I_{\mathrm{lim}}\Big/\sqrt{R_{\mathrm{F}}^2+X_{\mathrm{g2}}^2} < 0 \\ H_{\mathrm{eSC-ac}}(-\pi/2-\varphi_1) = \max\{P_{\mathrm{F}}^*\} \geq 0 \\ H_{\mathrm{eSC-dc}}(-\varphi_1) = -1.5X_{\mathrm{g2}}^2R_{\mathrm{F}}U_{\mathrm{g}}I_{\mathrm{lim}}\Big/\sqrt{R_{\mathrm{F}}^2+X_{\mathrm{g2}}^2} < 0 \\ H_{\mathrm{eSC-dc}}(-\pi/2-\varphi_1) = -0.75I_{\mathrm{lim}}^2X_{\mathrm{g}} - k_1\pi + k_1\varphi_1. \end{cases} \tag{60}$$

In (60), the value of $H_{\mathrm{SC\text{-}dc}}(-\pi/2-\varphi_1)$ cannot be determined. By applying the constraint: $H_{\mathrm{SC\text{-}dc}}(-\pi/2-\varphi_1) > 0$, the coefficient k_1 should satisfies (61) by considering the constraint: $\varphi_1 > 0$ in (41)

$$k_1 < \min\left\{-0.75I_{\mathrm{lim}}^2X_{\mathrm{g}}/(\pi-\varphi_1)\right\} = -0.75I_{\mathrm{lim}}^2X_{\mathrm{g}}/\pi. \tag{61}$$

Then, the uniqueness of the zero crossing point in $H_{\mathrm{eSC}}(\delta)$ among $(-\pi/2-\varphi_1, -\varphi_1)$ is demonstrated as (62)**.** It means that only one SEP exist among $(-\pi/2-\varphi_1, -\varphi_1)$ during type-II fault

$$\begin{cases} H_{\mathrm{eSC}}(-\varphi_1) = H_{\mathrm{eSC-dc}}(-\varphi_1) + H_{\mathrm{eSC-ac}}(-\varphi_1) < 0 \\ H_{\mathrm{eSC}}\left(-\frac{\pi}{2}-\varphi_1\right) = H_{\mathrm{eSC-dc}}\left(-\frac{\pi}{2}-\varphi_1\right) \\ +H_{\mathrm{eSC-ac}}\left(-\frac{\pi}{2}-\varphi_1\right) > 0 \end{cases}. \tag{62}$$

For the second condition: $\delta_{\mathrm{S}} < \delta_{\mathrm{ZC1}}$, considering $\mathrm{d}P_{\mathrm{eCS\text{-}SC}}/\mathrm{d}\delta > 0$ and $P_{\mathrm{eCS}} > 0$, the SEP may be located among $(\delta_{\mathrm{ZC2}}+2\pi, 2\pi-\varphi_1)$. Obviously, $H_{\mathrm{eSC}}(\delta)$ keeps monotonically decreasing among $(3\pi/2-\varphi_1, 2\pi-\varphi_1)$. But $P_{\mathrm{F}}{}^*$ and $P_{\mathrm{eCS\text{-}SC}}$ keep monotonically increasing among $(\delta_{\mathrm{ZC2}}+2\pi, 3\pi/2-\varphi_1)$. To maintain the monotonic decreasing characteristics of $H_{\mathrm{eSC}}(\delta)$, the condition in (63) should be satisfied for the feedback gain k_3 based on (25), (39)–(40) and (56)–(58) to makes the $P^*{}_{\mathrm{F\text{-}wREB}}$ as a monotonically decreasing function among $(\delta_{\mathrm{ZC2}}+2\pi, 3\pi/2-\varphi_1)$

$$\frac{\mathrm{d}P_{\mathrm{F-wREB}}^*(\delta)}{\mathrm{d}\delta} = -k_3 + \frac{3R_{\mathrm{F}}U_{\mathrm{g}}I_{\mathrm{lim}}k\cdot\cos(\varphi_1+\delta)}{2\sqrt{R_{\mathrm{F}}^2+X_{\mathrm{g2}}^2}} < 0. \tag{63}$$

Based on (63), the design criterion for coefficient k_3 should satisfy (64) by considering the constraint in (52). Moreover, the $\cos(\delta-\varphi_1)$ is scaled to 1 to obtain the largest changing rate

$$k_3 > 1.5kU_{\mathrm{g}}I_{\mathrm{lim}}. \tag{64}$$

Then, the $H_{\mathrm{eSC}}(\delta)$ can be maintained as a monotonic decreasing function among $(\delta_{\mathrm{ZC2}}+2\pi, 2\pi-\varphi_1)$.

Based on (25), (39)–(40), and (55)–(57), $H_{\mathrm{eSC}}(\delta_{\mathrm{ZC2}}+2\pi)$ and $H_{\mathrm{eSC}}(2\pi-\varphi_1)$ satisfy (65)–(66), It means that there exist and only exist one SEP among $(\delta_{\mathrm{ZC2}}+2\pi, 2\pi-\varphi_1)$ when the robust enhanced branch is introduced during type-II fault

$$H_{\mathrm{eSC}}(2\pi+\delta_{ZC2}) = \underbrace{-k_3\cdot(\delta_{ZC2}+\pi/2)}_{>0} + \underbrace{P_{\mathrm{F}}^{**}}_{\geq 0} > 0 \tag{65}$$

$$H_{\mathrm{eSC}}(2\pi-\varphi_1) = \underbrace{-1.5I_{\mathrm{lim}}^2X_{\mathrm{g2}}^2R_{\mathrm{F}}\big/\left(R_{\mathrm{F}}^2+X_{\mathrm{g2}}^2\right)}_{<0} + \underbrace{k_2\cdot(\varphi_1-\pi/2)}_{<0} < 0. \tag{66}$$

3) Design of Feedback Coefficient: Under $\delta_{\mathrm{S}} < \delta_{\mathrm{ZC1}}$, the UEP will move from point d to d' by introducing the robust enhanced branch as Fig. 17(a). Then, the power angle at UEP d' is denoted as $\delta_d{}'$ that satisfies (67). δ_{d} is the power angle at UEP d. The left boundary for the extra deceleration area is shortened to $-\pi$ as (68) to prevent the possible over calculation of deceleration area

$$\delta_{\mathrm{d}'} < \delta_{\mathrm{d}}, \delta_{\mathrm{d}} = \delta_{\mathrm{ZC1}} - 2\pi \in (-2\pi, -\pi) \tag{67}$$

$$D_{\mathrm{REB-cal}} + D_{\mathrm{REB-m}} \geq D_{\mathrm{REB-cal}} = \int_{-\pi}^{-\pi/2} P_{\mathrm{REB}}^*\mathrm{d}\delta \tag{68}$$

where the $D_{\mathrm{REB\text{-}cal}}$ denotes the calculated deceleration effect, the $D_{\mathrm{REB\text{-}m}}$ denotes the deceleration effect without calculation, which further increase the transient stability margin. The deceleration area provided by the robust enhanced branch should be larger than the extra acceleration area in (48) as

$$D_{\mathrm{REB-cal}} \geq A_{\mathrm{S}} + A_{\mathrm{CC}} - D_{\mathrm{EC}}. \tag{69}$$

Based on (48), (68)–(69), the boundary of k_1 is derived as

$$k_1 \leq -12I_{\mathrm{lim}}^2X_{\mathrm{g}}/\pi. \tag{70}$$

Under $\delta_{\mathrm{S}} > \delta_{\mathrm{ZC1}}$, the UEP will move from point d to d'' with the impact of the robust enhanced branch, the power angle at UEP d'' will be larger 2π. The right boundary of the deceleration area is scaled as 2π and the extra deceleration area provided by the robust enhanced branch is calculated as

$$D_{\mathrm{REB2-cal}} + D_{\mathrm{REB2-m}} - A_{\mathrm{REB2-cal}} \geq D_{\mathrm{REB2-cal}} - A_{\mathrm{REB2-cal}} = \int_{3\pi/2}^{2\pi} P_{\mathrm{REB}}^*\mathrm{d}\delta - \int_{\pi/2}^{3\pi/2} P_{\mathrm{REB}}^*\mathrm{d}\delta \tag{71}$$

where the $D_{\mathrm{REB2\text{-}cal}}$ denotes the calculated deceleration effect, the $D_{\mathrm{REB2\text{-}m}}$ denotes the deceleration effect without calculation, which further increase the transient stability margin. $A_{\mathrm{REB2\text{-}cal}}$ denotes the extra acceleration area among $(\pi/2, 3\pi/2)$.

The deceleration area introduced by the robust enhanced branch should be larger than the largest extra acceleration effect in (54) as

$$A_{\mathrm{CC2}} + A_{\mathrm{CC2S}} \leq D_{\mathrm{REB2-cal}} - A_{\mathrm{REB2-cal}}. \tag{72}$$

Based on (54) and (71)–(72), the k_2 should be designed as

$$k_2 \geq \left(12kU_{\mathrm{g}}I_{\mathrm{lim}} + 2\pi^2k_3\right)/\pi^2. \tag{73}$$

Based on the aforementioned design, the extra acceleration effect under type-II fault can be mitigated and the transient stability can be enhanced. The modified hybrid power synchronization scheme still can be applied to the Type-I fault condition to achieve dynamic power compensation because the power reference in (59) is still partly related to the grid voltage U_{g} on the connected point.

It also should be noted that the proposed robust enhanced method can also be applied under type-I fault. Fig. 18 further shows the acceleration and deceleration area distribution under type-I fault when robust enhanced branch is introduced with negative impedance measurement error. The UEP will move from point d to point d', the extra deceleration area is expanded

TABLE II
COMPARISON OF EXISTING ADVANCED TRANSIENT STABILITY ENHANCED METHODS

Method \ Performance	Robustness against parameters variation	Adaptivity to GFM control with virtual inertia	Free of fault depth detection	Dynamic Power compensation
Damping/ inertia optimization in [13]	×	√	√	×
q-axis voltage feedforward in [19]	×	×	√	√
Reactive power synchronization in [25]	√	×	√	×
Grid-code based control in [24]	√	√	×	√
Mode adaptive control in [16]	×	√	√	×
Power angle estimation in [18]	×	×	√	×
Frequency feedforward in [14]-[15]	×	√	√	×
Proposed Hybrid power synchronization in this paper	√	√	√	√

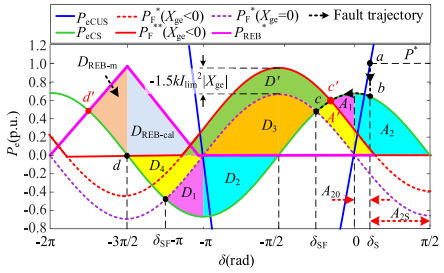

Fig. 18. Transient stability analysis under type-I fault with robust enhanced branch under negative impedance measurement error condition.

in $D_{\text{REB-cal}}$ and $D_{\text{REB-m}}$. The original balance between the deceleration area in D_1–D_4, D' and the acceleration area A_1, A_2, and A' is not violated in Section III-C. The condition under positive impedance measurement error is also similar. Owing to the limit pages, it is not illustrated in detail. In summary, the proposed hybrid power synchronization mechanism can be applied both under the two types of grid fault and there is no need for fault types detection.

Moreover, in design of k_1, k_2, and k_3, the (61), (64), (70), and (73) also can be design by considering the largest positive impedance measurement error as $X_{\text{gm}} = X_{\text{g}} + |X_{\text{ge}}|$.

D. Comparison of Existing Advanced Transient Stability Enhanced Methods

The performance of the existing transient stability enhanced control methods is compared from four perspectives as Table II.

1) Robustness against parameters variation. The damping/ inertia optimization method in [13], mode adaptive control in [16], and frequency feedforward in [14] and [15] cannot construct a SEP during grid fault or is highly relies on numerical analysis, leading to instability under change of fault clearing time, fault depth, and inaccurate grid impedance measurement.
2) Adaptivity to the GFM control with virtual inertia. The deceleration effect is not considered when it is designed for droop control with no virtual inertia in [17], [19], and [25]. Therefore, it may deteriorate the transient stability if it is directly applied in GFM control with virtual inertia.
3) Capability for fault depth detection free. The fault depth is hard to test online, which may cause low accuracy and long estimation time. Therefore, the method in [24] may be undesired for quick response during grid fault.
4) Dynamic power compensation capability. The method in [13], [14], and [15] that only with fixed active power output capability and the method in [25] only with fixed reactive power compensation capability is undesired.

Based on the four indexes, the proposed hybrid power synchronization method shows better performance. Moreover, the proposed method is suitable for a wide range of grid strength owing to the overcalculation of acceleration effect. Also, the proposed method can be applied both under line-to-ground fault and the voltage dip fault condition.

It should be noted that proposed hybrid power synchronization is designed by changing the active power reference based on reactive power feedback branch, which is different from the hybrid synchronization in [31] that based on voltage feedback loop by changing the equivalent damping.

V. SIMULATION AND EXPERIMENTAL VERIFICATION

The simulation and experimental verification are carried out in this section to demonstrate the aforementioned analysis.

A. Simulation Verification

To get an intuitive view of the analysis results, the proposed strategy is first verified used simulation by MATLAB&Simulink 2020b. The reactive power feedback coefficient k is set as $k = 1$ in the following simulation scenario. The parameters of GFM-VSC are given as Table I.

In Fig. 19(a)–(c), the grid impedance is set as 4.5 mH and the original power angle δ_{S} is about 0.31 rad. The grid voltage is set to drops to 0.2 p.u. and the impedance measurement error is set as -40%, 0%, and $+40\%$, the power angle is controlled nearly as $\delta_{\text{SF}} \approx -0.26$ rad, -0.78 rad, -1.32 rad, which corresponds to the analysis result that the negative grid impedance measurement error will lead to lift in the power angle at faulty SEP c' and the positive grid impedance measurement error will lead to decrease in the power angle at faulty SEP c''.

In Fig. 19(d), the fault depth is set as 50% voltage sags, the active and reactive power is about 0.75 p.u. and 1.21 p.u. Compared with the condition under 80% voltage drops in Fig. 19(a) that the active and reactive power is about 0.4 p.u. and 0.8 p.u., the dynamic power compensation under different fault depth is achieved.

Fig. 19(e)–(f) shows the simulation results when the grid impedance is set as 9 mH (short circuit ratio is about 1.35), the nominal power angle is about 0.68 rad, the grid voltage

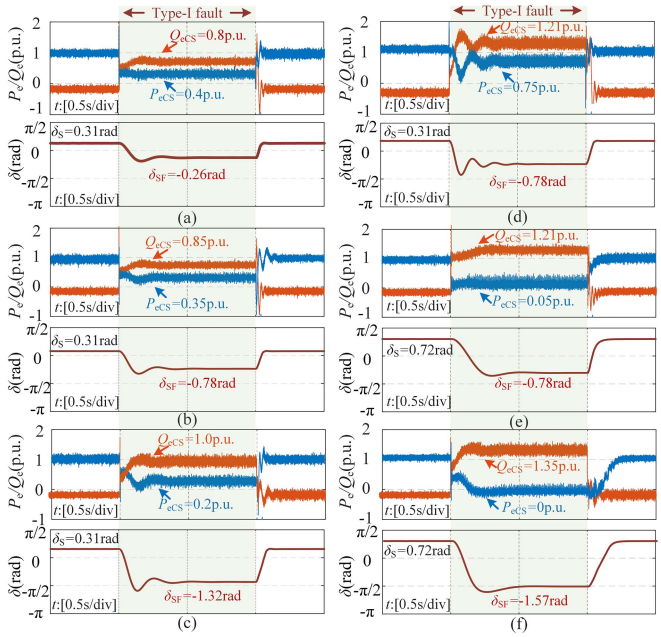

Fig. 19. Waveform of GFM-VSC under Type-I fault. (a) X_{ge}/X_g = -40% under U_{gF} = 0.2 p.u. and X_g = 4.5 mH. (b) X_{ge}/X_g = 0% under U_{gF} = 0.2 p.u. and X_g = 4.5 mH. (c) X_{ge}/X_g = +40% under U_{gF} = 0.2 p.u. and X_g = 4.5 mH. (d) X_{ge}/X_g = -40% under U_{gF} = 0.5 p.u. and X_g = 4.5 mH. (e) X_{ge}/X_g = -40% under U_{gF} = 0.2 p.u. and X_g = 9 mH. (f) X_{ge}/X_g = +40% under U_{gF} = 0.2 p.u. and X_g = 9 mH.

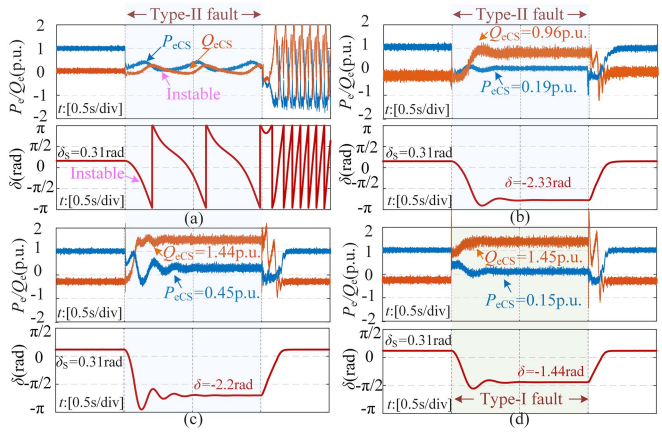

Fig. 20. Waveform of GFM-VSC under Type-II fault. (a) Without robust enhanced branch. (b) With robust enhanced branch under X_{g1} = 4.5 mH, X_{g2} = 1.5 mH. (c) With robust enhanced branch under X_{g1} = 1.5 mH, X_{g2} = 4.5 mH. (d) With robust enhanced branch under type-I fault (80% voltage sags).

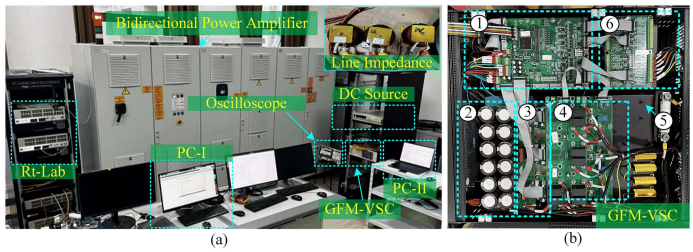

Fig. 21. PHIL experimental platform of GFM-VSC. (a) Envelope view. (b) Zoom-in view of GFM-VSC.

is set to drops to 0.2 p.u. When grid impedance measurement error is set as 0%, the faulty power angle is controlled nearly as $\delta_{SF} \approx -0.78$ rad. When +40% grid impedance measurement error is applied, the too large positive grid impedance measurement error will lead to the negative intersection point. The power reference limiter can effectively limit the negative power reference as 0 p.u. The active and reactive power is controlled as 0 p.u. and 1.35 p.u. The increase in reactive power (compared with the condition X_g = 4.5 mH) is because that the large grid impedance will lead to a high inner voltage in GFM-VSC under a same current limitation value, then the power support capability is increased. Overall, the hybrid power synchronization method shows high robustness in transient stability against impedance measurement error under different fault depth and grid strength condition. The dynamic power compensation is achieved without fault depth detection.

Fig. 20 further shows the waveform of GFM-VSC under type-II fault. The $R_F = 0.5\ \Omega$, the $X_{g1} = 1.5$ mH, and $X_{g2} = 4.5$ mH is set. Owing to the limit pages, the $\delta_S < \delta_{zc1}$ condition is tested. When the conventional hybrid power synchronization method is adopted, the transient instability problem occurred in Fig. 20(a), the fault resistance R_F is set as 0.5 Ω, the power angle keeps decreasing and finally enter into oscillation, which satisfies the analysis in Section V-B that the dc offset in active power will lead to the increase in acceleration area and cause the instability problem.

In Fig. 20(b), when the modified hybrid power synchronization method is adopted, the GFM-VSC can maintain as stable. Compared with the condition under Type-I fault, the power angle at the faulty SEP is much lower, which result from the phase shift φ_1 introduced under type-II fault.

In Fig. 20(c), the X_{g1} and X_{g2} is set as 4.5 mH and 1.5 mH, both the reactive and active power compensation value is improved because the increase in X_{g2} will lead to the increase in the amplitude of $P_{eCS\text{-}SC\text{-}ac}$ and $Q_{eCS\text{-}SC\text{-}ac}$. Therefore, the dynamic power compensation is also achieved.

In Fig. 20(d), the modified hybrid power synchronization method is tested under type-I fault. The U_{gF} is set as 0.2 p.u., the transient stable operation is also achieved, which means that the proposed method can be applied under different type of grid fault, the robustness of GFM-VSC is enhanced and there is no need to determine the fault types during fault inception.

B. Power-Hardware-in-Loop Experimental Verification

A 5 kW power-hardware-in-loop (PHIL) experimental platform has been established as Fig. 21. The corresponding functional scheme of the PHIL experimental platform is shown in Fig. 22. The PC-I is used to set the fault duration time and fault depth model based on MATLAB&Simulink software. The modeling step size is 0.000025 s. The RT-LAB (OP5707) is used to build this model and transfer it to the bidirectional power amplifier (EGSTON CSU200–1GAMP6-HV). The power amplifier (PA) is controlled as a bidirectional ac voltage source

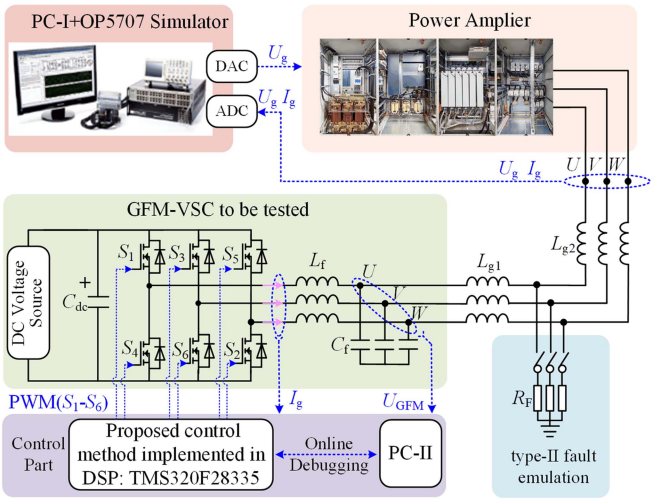

Fig. 22. Functional scheme of the PHIL experimental platform.

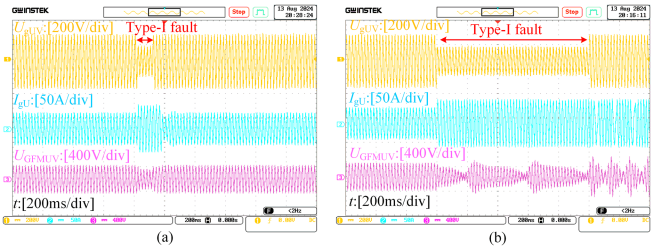

Fig. 23. Experimental waveforms of GFM-VSC with conventional control. (a) 100 ms voltage sags. (b) 1 s voltage sags.

to emulate the power grid. Three inductances are connected to the output port of the PA to emulate the grid impedance. The PC-II is used for executing the proposed control method in the digital signal processor (DSP) in the VSC. The detailed topology of GFM-VSC is shown in Fig. 20(b), includes: ① DSP (TMS320F28335); ② DC-Bus capacitance; ③ IGBT module; ④ Current and Voltage sensor; ⑤ *LC* filter; ⑥ Sampling board. The dc voltage source (IT6018D-1500-40) is set to provide constant dc voltage for the GFM-VSC. The Oscilloscope (Gwinstek GDS-2304A) is used for waveform recording. The parameters of the experimental platform are same with Table I.

Fig. 23(a) and (b) first shows the performance of conventional active power synchronization control. The grid voltage is set to drops to 0.5 p.u. and the fault duration time is set as 100 ms and 1 s. In Fig. 23(a), no oscillation problem in the output voltage U_{GFM} occur, which means that the GFM-VSC is stable. When the fault duration time is prolonged to 1 s, the oscillation in output voltage U_{GFM} occurred, which means that the transient instability problem occurred. Therefore, the conventional GFM control cannot withstand long time grid fault owing to the lack of SEP.

Fig. 24 shows the performance of the hybrid power synchronization control method for GFM-VSC under 50% grid voltage drop condition. The grid impedance measurement error is set as 0 mH. Compared with the conventional active power synchronization method in Fig. 23(b), no oscillation phenomenon in the

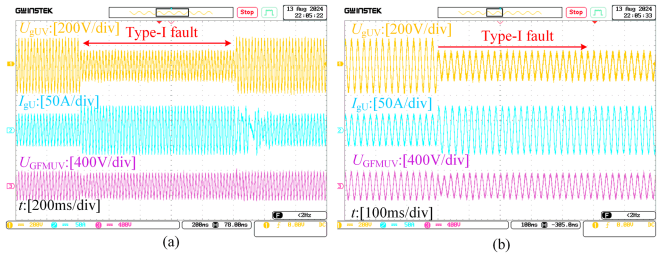

Fig. 24. Waveforms of GFM-VSC under 50% voltage sags and 0% grid impedance measurement error. (a) Envelop view. (b) Zoom-in view.

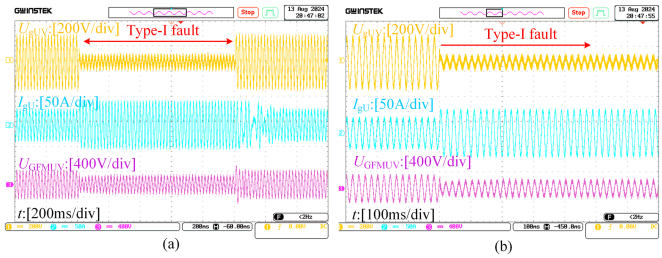

Fig. 25. Waveforms of inverter under 80% voltage sags and +40% grid impedance measurement error. (a) Envelop view. (b) Zoom-in view.

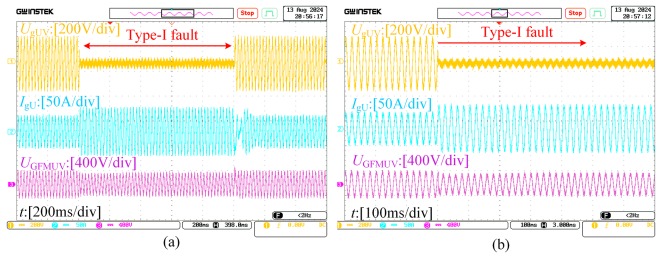

Fig. 26. Experimental results of GFM-VSC under line impedance equals to 10 mH and 90% grid fault. (a) Envelop view. (b) Zoom-in view.

output voltage of GFM-VSC occurred, which means that the transient stability is guaranteed.

Fig. 25 further shows the waveforms of GFM-VSC with the proposed hybrid power synchronization method under 80% grid voltage drop. The grid impedance measurement error is set as +40%. No oscillation phenomenon in output voltage occurred, which means that the proposed hybrid power synchronization method can enhance the transient stability of GFM-VSC under different fault depth without fault depth detection. The robustness against impedance measurement error is also high.

To test the effectiveness of the proposed transient stability enhanced method under different grid strength, the line inductance is increased to 9 mH and the grid impedance error is set as −4 mH (−40%), the corresponding short circuit ratio is about 1.35, and the grid voltage sags is set to drops to 0.1 p.u. No oscillation phenomenon occurred in the output voltage in GFM-VSC as Fig. 26. Therefore, the transient stability is guaranteed. It can be concluded that the proposed hybrid power synchronization method shows high adaptability to the change of grid strength. Moreover, extra transient stability margin in GFM-VSC is

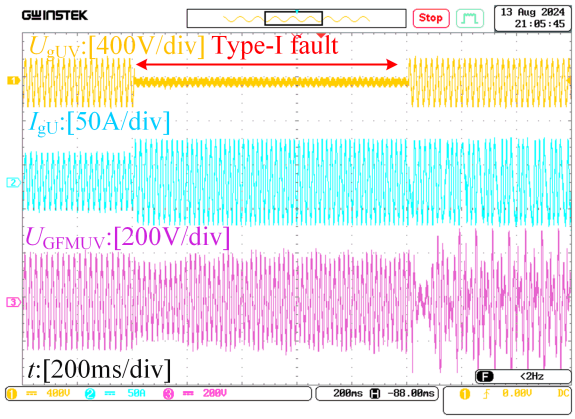

Fig. 27. Verification of the reactive power feedback coefficient k design.

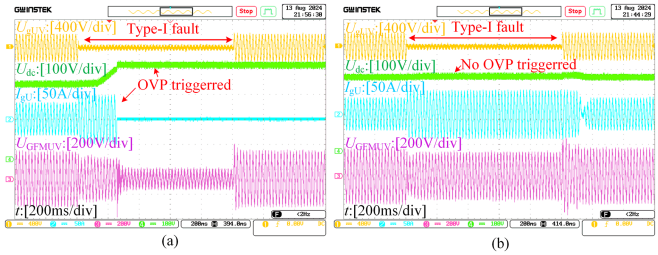

Fig. 28. Verification of the equivalent power reference limiter. (a) With power reference limiter. (b) Without power reference limiter.

guaranteed even the fault depth is lower than the designed lowest fault depth(0.2 p.u.) because the work of positive damping is not considered, which further enlarge the transient stability margin.

The design of the power feedback coefficient k for robustness enhancement against negative impedance measurement error is tested in Fig. 27. The coefficient k is set as 3 and -40% grid impedance measurement error is applied, which is higher than the upper boundary as 1.7 designed in Fig. 9. The oscillation problem occurred in the output voltage U_{GFM}. It means that the transient instability problem occurred in the GFM-VSC when the reactive power feedback gain k is higher than the designed upper boundary. The effectiveness in the design of power feedback coefficient k is demonstrated.

The effectiveness of the equivalent power reference limitation method is tested in Fig. 28 for robustness enhancement against positive impedance measurement error. The grid impedance measurement error is set as $+40\%$. In Fig. 28(a), no reference limiter is adopted, the dc-link overvoltage occurred in GFM-VSC, then the inverter blocked out. The current is stop to inject into the power grid, then the sampled ac side voltage is clamped by the faulty voltage of the power grid. The VSC is not blocked in the sudden of fault occurred because the slow dynamic of the power loop. It makes the GFM-VSC took about 270 ms to move to the operating point that with a negative power reference. When the reference limiter is adopted in Fig. 28(b), no overvoltage occurred and the GFM-VSC can maintain in synchronization with the grid. It is demonstrated that the introduction of power reference limiter can increase the robustness of the hybrid power synchronization method against positive grid impedance measurement error.

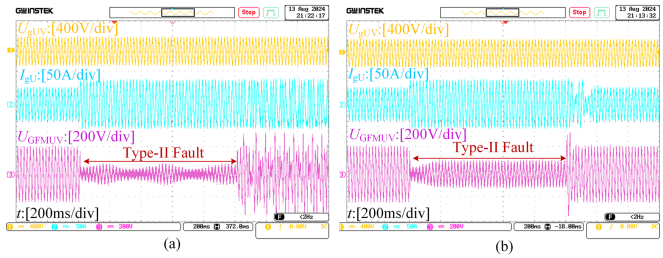

Fig. 29. Verification of the modified hybrid power synchronization method under type-II fault. (a) Without robust enhanced branch. (b) With robust enhanced branch.

The effectiveness of the hybrid power synchronization method with robust enhanced branch under type-II fault is tested in Fig. 29. The fault resistance R_{F} is set as 0.5 Ω. When robust enhanced branch is not adopted, the oscillation in output voltage occurred. It means that the transient instability problem occurred under the first condition in Section IV, A that $\delta_{\mathrm{S}} > \delta_{\mathrm{ZC1}}$, the dc offset in the active power will lead to the increase in acceleration area and further cause instability problem. When the robust enhanced branch is introduced, the stable operation of GFM-VSC is achieved, which means that the extra acceleration area introduced by the dc offset in the active power is successfully mitigated by the robust enhanced branch.

VI. Conclusion

The conventional transient stable operation of GFM-VSC is highly sensitive to parameter variation and measurement accuracy. In this article, the hybrid power synchronization method is proposed to enhance robustness of transient stability against parameters variation. The reactive power is introduced as the equivalent dynamic power reference that internally related to fault depth, then the dynamic power compensation without fault depth detection is achieved. The reactive power feedback gain tuning and reference limitation method is introduced to make sure the SEP exist under large impedance measurement error. The EAC analysis shows that the hybrid power synchronization based GFM-VSC always get extra deceleration area left under over-calculation of acceleration effect. It enables the GFM-VSC with virtual inertia shows high robustness in transient stability against parameters variation and different grid strength. The impact of short circuit fault in the transmission line on transient stability of the proposed method is also analyzed and the robust enhancement method is also given. The simulation and experimental results verified the effectiveness of the proposed control method. The future work includes the impact of negative sequence current injection during asymmetric grid fault on transient stability and its optimal control method and the optimal reactive power feedback coefficient design method in low inertia system.

Appendix

The $P_{\mathrm{eCS\text{-}SC\text{-}dc}}$ in (39) can be viewed as a function with respect to fault resistance R_{F}, which can be rewritten as

$$P_{\mathrm{eCS-SC-dc}} = 1.5 I_{\mathrm{lim}}^2 X_{\mathrm{g2}}^2 / g\left(R_{\mathrm{F}}\right), g(R_{\mathrm{F}}) = R_{\mathrm{F}} + X_{\mathrm{g2}}^2 / R_{\mathrm{F}}. \tag{74}$$

Based on (74), the derivative of $g(R_{\mathrm{F}})$ is derived as

$$\mathrm{d}g\left(R_{\mathrm{F}}\right)/\mathrm{d}R_{\mathrm{F}} = 1 - X_{\mathrm{g2}}^2/R_{\mathrm{F}}^2. \tag{75}$$

By applying the constraint: $\mathrm{d}g(R_{\mathrm{F}})/\mathrm{d}R_{\mathrm{F}} = 0$ in (75), the minimum value of $g(R_{\mathrm{F}})$ is calculated as

$$\left[g(R_{\mathrm{F}})\right]_{\min} = g(X_{\mathrm{g2}}) = 2X_{\mathrm{g2}}. \tag{76}$$

Then, the maximum value of the $P_{\mathrm{eCS\text{-}SC\text{-}dc}}$ can be calculated as (77) by applying the constraint that $X_{\mathrm{g2}} < X_{\mathrm{g}}$

$$P_{\mathrm{eCS-SC-dc}} \le 1.5I_{\mathrm{lim}}^2 X_{\mathrm{g2}}^2/\left[g\left(R_{\mathrm{F}}\right)\right]_{\min} < 0.75I_{\mathrm{lim}}^2 X_{\mathrm{g}}. \tag{77}$$

For the $Q_{\mathrm{eCS\text{-}SC\text{-}dc}}$ (dc offset component in the reactive power), it can be easy rewritten as

$$Q_{\mathrm{eCS-SC-dc}} = 1.5I_{\mathrm{lim}}^2\left[X_{\mathrm{g2}}/\left(1 + X_{\mathrm{g2}}^2/R_{\mathrm{F}}^2\right) + X_{\mathrm{g1}}\right]. \tag{78}$$

Because ${X_{\mathrm{g2}}}^2/{R_{\mathrm{F}}}^2 > 0$, therefore, the maximum value of $Q_{\mathrm{eCS\text{-}SC\text{-}dc}}$ can be derived as

$$Q_{\mathrm{eCS-SC-dc}} < 1.5I_{\mathrm{lim}}^2\left(X_{\mathrm{g2}} + X_{\mathrm{g1}}\right) = 1.5I_{\mathrm{lim}}^2 X_{\mathrm{g}}. \tag{79}$$

REFERENCES

[1] R. Rosso, X. Wang, M. Liserre, X. Lu, and S. Engelken, "Grid-forming converters: Control approaches, grid-synchronization, and future trends—A review," *IEEE Open J. Ind. Appl.*, vol. 2, pp. 93–109, 2021.

[2] T. Liu and X. Wang, "Unified voltage control for grid-forming inverters," *IEEE Trans. Ind. Electron.*, vol. 71, no. 3, pp. 2578–2589, Mar. 2024.

[3] S. Bhadoria et al., "Enablers for overcurrent capability of silicon-carbide-based power converters: An overview," *IEEE Trans. Power Electron.*, vol. 38, no. 3, pp. 3569–3589, Mar. 2023.

[4] T. Qoria, H. Wu, X. Wang, and I. Colak, "Variable virtual impedance-based overcurrent protection for grid-forming inverters: Small-signal, large-signal analysis and improvement," *IEEE Trans. Smart Grid*, vol. 14, no. 5, pp. 3324–3336, Sep. 2023.

[5] H. Wu, X. Wang, and L. Zhao, "Design considerations of current-limiting control for grid-forming capability enhancement of VSCs under large grid disturbances," *IEEE Trans. Power Electron.*, vol. 39, no. 10, pp. 12081–12085, Oct. 2024.

[6] B. Fan and X. Wang, "Equivalent circuit model of grid-forming converters with circular current limiter for transient stability analysis," *IEEE Trans. Power Syst.*, vol. 37, no. 4, pp. 3141–3144, Jul. 2022.

[7] B. Fan and X. Wang, "Fault recovery analysis of grid-forming inverters with priority-based current limiters," *IEEE Trans. Power Syst.*, vol. 38, no. 6, pp. 5102–5112, Nov. 2023.

[8] B. Fan, T. Liu, F. Zhao, H. Wu, and X. Wang, "A review of current-limiting control of grid-forming inverters under symmetrical disturbances," *IEEE Open J. Power Electron.*, vol. 3, pp. 955–969, 2022.

[9] J. Lei, X. Xiang, W. Li, and X. He, "The analysis and calculation of power angle dynamics in grid forming converter under large disturbances based on kbm asymptotic method," *IEEE Trans. Power Electron.*, vol. 38, no. 2, pp. 1494–1508, Feb. 2023.

[10] G. Wang, L. Fu, Q. Hu, C. Liu, and Y. Ma, "Transient synchronization stability of grid-forming converter during grid fault considering transient switched operation mode," *IEEE Trans. Sustain. Energy*, vol. 14, no. 3, pp. 1504–1515, Jul. 2023.

[11] J. Lei, X. Xiang, B. Liu, W. Li, and X. He, "Quantitative and intuitive VSG transient analysis with the concept of damping area approximation," *IEEE Trans. Smart Grid*, vol. 14, no. 3, pp. 2477–2480, May 2023.

[12] J. Lei, X. Xiang, B. Liu, W. Li, and X. He, "Transient stability analysis of grid forming converters based on damping energy visualization and geometry approximation," *IEEE Trans. Ind. Electron.*, vol. 71, no. 3, pp. 2510–2521, Mar. 2024.

[13] P. Ge, C. Tu, F. Xiao, Q. Guo, and J. Gao, "Design-oriented analysis and transient stability enhancement control for a virtual synchronous generator," *IEEE Trans. Ind. Electron.*, vol. 70, no. 3, pp. 2675–2684, Mar. 2023.

[14] M. Chen, D. Zhou, and F. Blaabjerg, "Enhanced transient angle stability control of grid-forming converter based on virtual synchronous generator," *IEEE Trans. Ind. Electron.*, vol. 69, no. 9, pp. 9133–9144, Sep. 2022.

[15] X. Xiong, C. Wu, and F. Blaabjerg, "An improved synchronization stability method of virtual synchronous generators based on frequency feedforward on reactive power control loop," *IEEE Trans. Power Electron.*, vol. 36, no. 8, pp. 9136–9148, Aug. 2021.

[16] H. Wu and X. Wang, "A mode-adaptive power-angle control method for transient stability enhancement of virtual synchronous generators," *IEEE J. Emerg. Sel. Topics Power Electron.*, vol. 8, no. 2, pp. 1034–1049, Jun. 2020.

[17] E. Rokrok, T. Qoria, A. Bruyere, B. Francois, and X. Guillaud, "Transient stability assessment and enhancement of grid-forming converters embedding current reference saturation as current limiting strategy," *IEEE Trans. Power Syst.*, vol. 37, no. 2, pp. 1519–1531, Mar. 2022.

[18] R. Sun, J. Ma, W. Yang, S. Wang, and T. Liu, "Transient synchronization stability control for LVRT with power angle estimation," *IEEE Trans. Power Electron.*, vol. 36, no. 10, pp. 10981–10985, Oct. 2021.

[19] L. Huang, H. Xin, Z. Wang, L. Zhang, K. Wu, and J. Hu, "Transient stability analysis and control design of droop-controlled voltage source converters considering current limitation," *IEEE Trans. Smart Grid*, vol. 10, no. 1, pp. 578–591, Jan. 2019.

[20] T. Qoria, F. Gruson, F. Colas, G. Denis, T. Prevost, and X. Guillaud, "Critical clearing time determination and enhancement of grid-forming converters embedding virtual impedance as current limitation algorithm," *IEEE J. Emerg. Sel. Topics Power Electron.*, vol. 8, no. 2, pp. 1050–1061, Jun. 2020.

[21] H. Wu and X. Wang, "Design-oriented transient stability analysis of grid-connected converters with power synchronization control," *IEEE Trans. Ind. Electron.*, vol. 66, no. 8, pp. 6473–6482, Aug. 2019.

[22] H. Wu and X. Wang, "Control of grid-forming VSCs: A perspective of adaptive fast/slow internal voltage source," *IEEE Trans. Power Electron.*, vol. 38, no. 8, pp. 10151–10169, Aug. 2023.

[23] J. Fang, H. Deng, and S. M. Goetz, "Grid impedance estimation through grid-forming power converters," *IEEE Trans. Power Electron.*, vol. 36, no. 2, pp. 2094–2104, Feb. 2021.

[24] T. Liu, X. Wang, F. Liu, K. Xin, and Y. Liu, "A current limiting method for single-loop voltage-magnitude controlled grid-forming converters during symmetrical faults," *IEEE Trans. Power Electron.*, vol. 37, no. 4, pp. 4751–4763, Apr. 2022.

[25] H. Deng, Y. Qi, J. Fang, Y. Tang, and V. Debusschere, "A robust low-voltage-ride-through strategy for grid-forming converters based on reactive power synchronization," *IEEE Trans. Power Electron.*, vol. 38, no. 1, pp. 346–357, Jan. 2023.

[26] L. Harnefors, M. Hinkkanen, U. Riaz, F. M. M. Rahman, and L. Zhang, "Robust analytic design of power-synchronization control," *IEEE Trans. Ind. Electron.*, vol. 66, no. 8, pp. 5810–5819, Aug. 2019.

[27] Z. Kustanovich, S. Shivratri, H. Yin, F. Reissner, and G. Weiss, "Synchronverters with fast current loops," *IEEE Trans. Ind. Electron.*, vol. 70, no. 11, pp. 11357–11367, Nov. 2023.

[28] F. Cecati, M. Liserre, Y. Liao, X. Wang, and F. Blaabjerg, "Design oriented analysis of control loops interaction in power synchronization-based voltage source converter," in *Proc. IEEE Energy Convers. Congr. Expo.*, Vancouver, BC, Canada, 2021, pp. 3282–3288.

[29] "Technical requirements for grid connection of distributed resources," Standardization Administration of China, China, Tech. Rep. GB/T 33593-2017, 2017.

[30] Z. Shuai, C. Shen, X. Liu, Z. Li, and Z. J. Shen, "Transient angle stability of virtual synchronous generators using Lyapunov's direct method," *IEEE Trans. Smart Grid*, vol. 10, no. 4, pp. 4648–4661, Jul. 2019.

[31] T. Liu and X. Wang, "Physical Insight into hybrid-synchronization-controlled grid-forming inverters under large disturbances," *IEEE Trans. Power Electron.*, vol. 37, no. 10, pp. 11475–11480, Oct. 2022.

Pengfei Sun was born in Zibo, China, in 1997. He received the B.S. degree from the Harbin University of Science and Technology, Harbin, China, in 2019, and the M.S. degree from the Harbin Institute of Technology, Harbin, China, in 2021, both in electrical engineering. Since 2022, he has been working toward the Ph.D. degree in electrical engineering with Wuhan University, Wuhan, China.

His research interests include simultaneous wireless power and data transfer, modeling, and control of grid-tied converter.

Zhen Tian (Member, IEEE) received the B.S. degree in electrical engineering from Wuhan University, Wuhan, China, in 2014, and the Ph.D. degree in control science and engineering from Shanghai Jiao Tong University, Shanghai, China, in 2019.

During 2017–2019, he was a visiting scholar with the Department of Electrical and Computer Engineering, Illinois Institute of Technology, Chicago, USA. He is currently a Postdoctoral Fellow with the School of Electrical Engineering and Automation, Wuhan University. His research interests mainly include modeling, control and stability analysis of renewable energy generation, microgrid, and power-electronics-enabled power systems.

Xiaoming Zha (Member, IEEE) was born in Huaining, China, in 1967. He received the B.S., M.S., and Ph.D. degrees in electrical engineering from Wuhan University, Wuhan, China, in 1989, 1992, and 2001, respectively.

He was a Postdoctoral Fellow with the University of Alberta, Canada, from 2001 to 2003. He has been a Faculty Member with Wuhan University since 1992, and became a Professor in 2003. He is currently the Deputy Dean with the School of Electrical Engineering, Wuhan University, Wuhan, China. His research interests include power electronic converter, the application of power electronics in smart grid and renewable energy generation, the analysis and control of microgrid, the analysis and control of power quality, and frequency control of high-voltage high-power electric motors.

Meng Huang (Member, IEEE) received the B.Eng. and M.Eng. degrees in electronic science and technology from the Huazhong University of Science and Technology, Wuhan, China, in 2006 and 2008, respectively, and the Ph.D. degree in electrical engineering from the Hong Kong Polytechnic University, Hong Kong, in 2013.

He is currently a Professor with the School of Electrical Engineering and Automation, Wuhan University, Wuhan, China. His research interests include nonlinear analysis of power converters and power electronics reliability.

Dr. Huang was the recipient of the best paper award of the IEEE TRANSACTIONS ON POWER ELECTRONICS in 2016. He is the Guest Associate Editor for the IEEE JOURNAL OF EMERGING AND SELECTED TOPICS OF POWER ELECTRONICS, IEEE JOURNAL OF EMERGING AND SELECTED TOPICS OF CIRCUITS AND SYSTEMS, and the Associate Editor for the IEEE ACCESS.

Yibin Tao received the B.S. degree from Anhui University, Hefei, China, and the M.S. and Ph.D. degrees in from South China University of Technology Guangzhou, China, in 2008 and 2022, respectively, all in electrical engineering.

He has been a R&D Engineer with China Electric Power Research Institute since 2008. He is currently the Director with the Energy Storage System Research Department. His research interests include modeling and control of the power electronic converter.

Chong Shao received B.S. and Ph.D. degrees in electrical engineering from Tsinghua University, Beijing, China, in 2006 and 2012, respectively.

He has been a Dispatch Engineer with State Grid Gansu Electric Power Company since 2012 and he is currently the Director with the System Operation Department, Power Dispatch Control Center, State Grid Gansu Electric Power Company, Beijing, China. His research interests include the safe control and operation of the power electronic converter and the dispatch of the large scaled power system.

Xiping Ma received the B.S. and M.S. degrees in electrical engineering from Beijing Jiaotong University, Beijing, China, in 2009 and 2012, respectively.

He has been a Dispatch Engineer with Electric Power Research Institute, State Grid Gansu Electric Power Company, since 2012 and he is currently the Director with the Distributed Power Generation and Microgrid Engineering Research Center, Electric Power Research Institute, State Grid Gansu Electric Power Company. His research interests include the modeling and analysis of the grid connected inverter used in distributed power generation system.